JEM Journal of Experimental Medicine

ARTICLE

Hypoxia is linked to acquired resistance to immune checkpoint inhibitors in lung cancer

Camila Robles-Oteíza[1], Katherine Hastings[2], Jungmin Choi[3,4], Isabelle Sirois[5], Arvind Ravi[6,7], Francisco Expósito[2], Fernando de Miguel[2], James R. Knight[8], Francesc López-Giráldez[8], Hyejin Choi[9], Nicholas D. Socci[10], Taha Merghoub[9,11,12], Mark Awad[13,14], Gad Getz[6,15,16], Justin Gainor[17], Matthew D. Hellmann[18], Étienne Caron[5,19], Susan M. Kaech[20], and Katerina Politi[2,21]

Despite the established use of immune checkpoint inhibitors (ICIs) to treat non-small cell lung cancer (NSCLC), only a subset of patients benefit from treatment and ∼50% of patients whose tumors respond eventually develop acquired resistance (AR). To identify novel drivers of AR, we generated murine *Msh2* knock-out (KO) lung tumors that initially responded but eventually developed AR to anti-PD-1, alone or in combination with anti-CTLA-4. Resistant tumors harbored decreased infiltrating T cells and reduced cancer cell-intrinsic MHC-I and MHC-II levels, yet remained responsive to IFNγ. Resistant tumors contained extensive regions of hypoxia, and a hypoxia signature derived from single-cell transcriptional profiling of resistant cancer cells was associated with decreased progression-free survival in a cohort of NSCLC patients treated with anti-PD-1/PD-L1 therapy. Targeting hypoxic tumor regions using a hypoxia-activated pro-drug delayed AR to ICIs in murine *Msh2* KO tumors. Thus, this work provides a rationale for targeting tumor metabolic features, such as hypoxia, in combination with immune checkpoint inhibition.

Introduction

Immune checkpoint inhibitors (ICIs) have become a first-line standard of care, in combination with chemotherapy, for many patients with advanced non-small cell lung cancer (NSCLC) (Borghaei et al., 2015; Brahmer et al., 2015; Reck et al., 2016; Planchard et al., 2018). However, only a subset of patients receive durable clinical benefit from these agents, and ∼50–60% of patients whose tumors initially respond eventually develop acquired resistance (AR) (Gettinger et al., 2018; Schoenfeld and Hellmann, 2020; Memon et al., 2024; Ricciuti et al., 2024). As increasing numbers of patients receive immune checkpoint inhibitor therapy, particularly in the first-line setting and during earlier stages of the disease, AR will continue to grow as a clinical challenge (Gettinger et al., 2018; Herbst et al., 2020). Thus, understanding the underlying mechanisms that allow tumors to escape during therapy is essential to inform strategies that can delay or overcome resistance.

Clinical studies of resistance to immune checkpoint inhibition have converged on the antigen presentation and interferon (IFN) signaling pathways as important mediators of resistance (Gettinger et al., 2017; Sade-Feldman et al., 2018; Zaretsky et al., 2016; Le et al., 2017; Sucker et al., 2017). Alterations in β-2 microglobulin (*B2M*), a component of the major histocompatibility complex (MHC) class I complex that is critical for its stable expression at the cell surface, have been identified in lung cancer, colorectal cancer, and melanoma with resistance to ICIs (Gettinger et al., 2017; Sade-Feldman et al., 2018; Zaretsky et al., 2016; Le et al., 2017). Loss-of-function mutations in *JAK1/2* were

[1]Department of Immunobiology, Yale School of Medicine, New Haven, CT, USA; [2]Yale Cancer Center, Yale School of Medicine, New Haven, CT, USA; [3]Department of Genetics, Yale School of Medicine, New Haven, CT, USA; [4]Department of Biomedical Sciences, Korea University College of Medicine, Seoul, Korea; [5]CHU Sainte-Justine Research Center, Montreal, Canada; [6]Broad Institute of Massachusetts Institute of Technology and Harvard, Cambridge, MA, USA; [7]Lank Center for Genitourinary Oncology, Dana-Farber Cancer Institute, Boston, MA, USA; [8]Yale Center for Genome Analysis, Yale University, New Haven, CT, USA; [9]Ludwig Collaborative and Swim Across America Laboratory, Memorial Sloan Kettering Cancer Center, New York, NY, USA; [10]Marie-Josee and Henry R. Kravis Center for Molecular Oncology, Memorial Sloan Kettering Cancer Center, New York, NY, USA; [11]Human Oncology and Pathogenesis Program & Parker Institute for Cancer Immunotherapy, Memorial Sloan Kettering Cancer Center, New York, NY, USA; [12]Department of Medicine, Weill Cornell Medical College, New York, NY, USA; [13]Lowe Center for Thoracic Oncology, Dana-Farber Cancer Institute, Boston, MA, USA; [14]Department of Medicine, Harvard Medical School, Boston, MA, USA; [15]Department of Pathology, Harvard Medical School, Boston, MA, USA; [16]Krantz Family Center for Cancer Research and Department of Pathology, Massachusetts Genral Hospital, Boston, MA, USA; [17]Center for Thoracic Cancers, Massachusetts General Hospital, Boston, MA, USA; [18]Department of Medicine, Memorial Sloan Kettering Cancer Center, New York, NY, USA; [19]Department of Pathology and Cellular Biology, Faculty of Medicine, Université de Montréal, Montreal, Canada; [20]NOMIS Center for Immunobiology and Microbial Pathogenesis, Salk Institute, La Jolla, CA, USA; [21]Departments of Pathology and Internal Medicine (Section of Medical Oncology), Yale School of Medicine, New Haven, CT, USA.

Correspondence to Katerina Politi: katerina.politi@yale.edu; Susan M. Kaech: skaech@salk.edu.

also identified in ICI-resistant melanoma, and these alterations rendered the tumors insensitive to IFNγ signaling, which can induce cancer cell MHC-I expression (Sucker et al., 2017). Subsequent studies using mouse models of lung cancer and melanoma with loss-of-function mutations in *B2m*, *Jak1*, and *Jak2* further confirmed the functional relevance of these mechanisms of ICI resistance (Gettinger et al., 2017; Kalbasi et al., 2020; Torrejon et al., 2020). For example, in *Jak1*-deficient tumors that were insensitive to IFNγ, restoration of cancer cell–intrinsic MHC-I expression rendered these tumors sensitive to adoptive T cell transfer or immune checkpoint blockade (Kalbasi et al., 2020; Torrejon et al., 2020). Although these genetic approaches to model resistance have produced strategies to overcome known drivers of resistance, they are less well suited to the identification of additional novel mediators of AR.

To address this challenge, we modeled AR to ICIs in a mouse model of lung adenocarcinoma that was genetically modified to have an increased tumor mutational burden (TMB). Elevated TMB, along with T cell infiltration and tumor PD-L1 expression, has been identified as a biomarker of response to ICIs across diverse cancer types (Tumeh et al., 2014; Rizvi et al., 2015; Samstein et al., 2019), consistent with the fact that nonsynonymous mutations can give rise to neoantigens that are recognized by T cells, the targets of immune checkpoint inhibition (Gubin et al., 2014; McGranahan et al., 2016). Tumors with DNA mismatch repair deficiencies (MMRd) accumulate somatic mutations, and their elevated TMB correlates with clinical responses to ICIs (Supek and Lehner, 2015; Le et al., 2017). As a result of this, MMRd is used as a biomarker to select patients for treatment with ICIs across indications (Le et al., 2015). However, not all MMRd tumors with elevated TMB respond to ICIs, highlighting that additional interrelated factors, including tumor type and the mechanisms driving mutagenesis, dictate clinical outcomes (Rousseau et al., 2021). Consistent with these findings, the deletion of core genes involved in DNA mismatch repair including *Msh2* and *Mlh1* has been successfully used in murine tumor models to increase their mutational burden, and in some cases, increase their sensitivity to ICIs (Germano et al., 2017; Mandal et al., 2019; Martinez-Usatorre et al., 2021; Westcott et al., 2023).

To investigate novel mechanisms of AR to ICIs, we used murine syngeneic *Msh2* knock-out (KO) lung adenocarcinoma models with elevated TMB to generate tumors that developed AR to anti-PD-1, either alone or in combination with anti-CTLA-4 (both clinically relevant in NSCLC). We identified hypoxia as a key feature of resistant tumors, studied its relevance in a cohort of NSCLC patients who were treated with ICIs, and identified an approach to delay the emergence of AR. Thus, by evaluating the genomic, transcriptional, and functional features that distinguished resistant tumors from those responding to therapy, we identified novel vulnerabilities that can be exploited using combinatorial therapeutic approaches.

Results

T cell–dependent response to ICIs in a TMB-high *Msh2* KO lung adenocarcinoma model

To generate lung adenocarcinoma cell lines with an increased TMB, we used CRISPR/*Cas9*-mediated genome editing to knock out the DNA mismatch repair enzyme *Msh2* in two $Kras^{G12D}$ driven lung cancer models, $p53^{WT}$ LKR13 (Wislez et al., 2005) and $p53^{flox/flox}$ 368T1 cells (Winslow et al., 2011) (Fig. 1 A, Fig. S1 A). Whole-exome sequencing (WES) of two KO single-cell clones from each line identified clones with a low (L) or high (H) number of non-synonymous single nucleotide variants (SNVs) relative to the empty vector (EV) control cells (Fig. 1 B). *Msh2* deficiency did not impair cell proliferation in vitro (Fig. S1 B). We evaluated the growth of EV and *Msh2* KO cells in immunocompromised nonobese diabetic (NOD) severe combined immunodeficient (SCID) $Il2rg^{-/-}$ (NSG) and $Rag1^{KO}$ mice and found no difference in the growth rate of EV and *Msh2* KO 368T1 tumors in either strain. In contrast, relative to EV tumors the LKR13 *Msh2* KO tumors had decreased growth rates in both NSG and $Rag1^{KO}$ animals, suggesting that the proliferation of these cells was impaired via an in vivo–specific tumor cell–intrinsic mechanism (Fig. S1 C). We also confirmed that LKR13 and 368T1 EV and *Msh2* KO cells expressed MHC-I and PD-L1 upon IFNγ stimulation (Fig. S1 D).

To evaluate ICI responses, immunocompetent mice bearing subcutaneous 368T1 and LKR13 EV and *Msh2* KO tumors were treated with anti-PD-1 + anti-CTLA-4 on day 10 after engraftment (average tumor volume 30–50 mm^3), and T cells were depleted with anti-CD4 and anti-CD8 antibodies starting 1 day prior to ICI treatment (Fig. 1 C). Although LKR13-EV and 368T1-EV tumors did not regress upon anti-PD-1 + anti-CTLA-4 treatment, *Msh2* KO LKR13-L and LKR13-H tumors demonstrated significant growth attenuation or regression, respectively, in a T cell–dependent manner (Fig. 1 D). In contrast, 368T1-L and 368T1-H tumors overall did not regress upon ICI treatment despite harboring TMBs similar to the LKR13 models (Fig. 1 D).

We next examined how increased TMB in *Msh2* KO tumors impacted the immune response to therapy. LKR13-L and LKR13-H tumors harbored increased $CD8^+$ T cells relative to LKR13-EV tumors, and in LKR13-H tumors $CD8^+$ T cells also increased after anti-PD-1 + anti-CTLA-4 therapy (Fig. 1 E). However, $CD8^+$ T cell abundance did not increase in 368T1-L and 368T1-H tumors (Fig. 1 E). IFNγ production after ex vivo stimulation was significantly higher in $CD8^+$ T cells from LKR13-L and LKR13-H tumors compared to those from LKR13-EV tumors, whereas $CD8^+$ T cell IFNγ production was not significantly altered in 368T1 tumors (Fig. 1 G). Despite no significant changes in $CD4^+$ T cell abundance in the LKR13 or 368T1 tumors (Fig. 1 F), IFNγ production after ex vivo stimulation was increased in $CD4^+$ T cells derived from LKR13-H, 368T1-L, and 368T1-H tumors (Fig. 1 H).

Collectively, the greatest increases in T cell abundance and IFNγ production occurred in LKR13-L and LKR13-H tumors, consistent with their T cell–dependent response to ICIs. T cell depletion also decreased surface PD-L1 expression on $CD45^-$ cancer (and stromal) cells from LKR13-L and LKR13-H tumors, but not 368T1-L and 368T1-H tumors (Fig. S1 E), consistent with the role of T cell–derived IFNγ in the induction of cancer cell PD-L1 expression in ICI-responsive tumors (Garcia-Diaz et al., 2017; Baumeister et al., 2016). Overall, the immune microenvironment of LKR13-L and LKR13-H tumors was consistent with these models' responsiveness to ICIs, in contrast with the non-responsive 368T1 models.

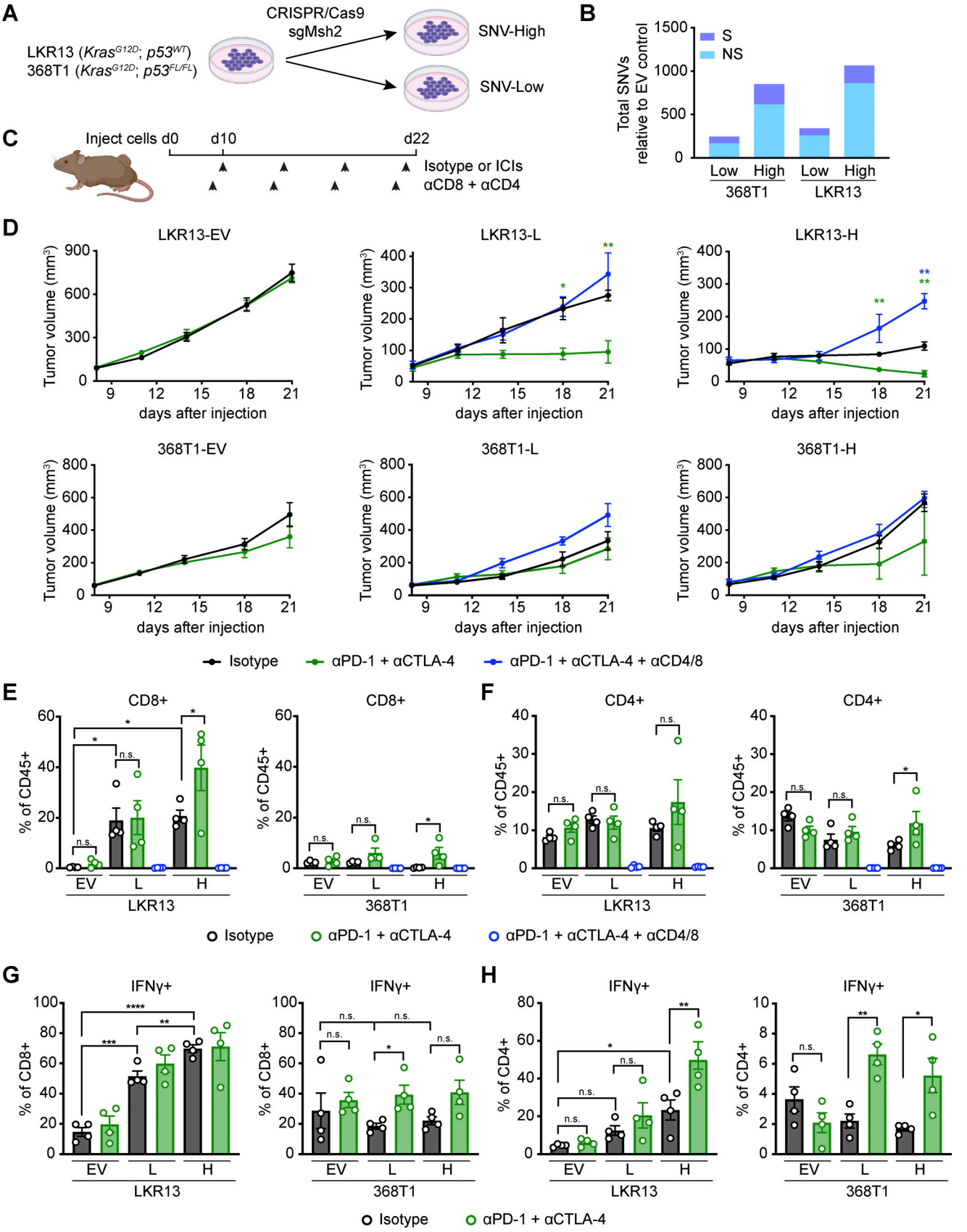

Figure 1. **Response to ICIs in *Msh2* KO LKR13 lung tumors is T cell dependent. (A)** Schematic of *Msh2* KO lung adenocarcinoma cell lines generated using CRISPR/*Cas9*. **(B)** Number of synonymous (S) and non-synonymous (NS) SNVs identified in four *Msh2* KO cell lines relative to EV controls. LKR13 and 368T1 *Msh2* KO cells were categorized as having H or L TMB. **(C)** Experimental strategy: subcutaneous tumors were treated with either Iso or anti-PD-1 and

anti-CTLA-4 twice weekly starting on day (d) 10 after tumor initiation, and T cells were depleted with anti-CD4 and anti-CD8 antibodies twice weekly starting on day 9. **(D)** Tumor growth curves after 500,000 of the indicated cells were injected subcutaneously into syngeneic B6129SF1/J mice (n = 4 mice per group). **(E–H)** Abundance of CD8$^+$ (E) and CD4$^+$ (F) T cells as a percentage of CD45$^+$ cells and IFNγ secretion after ex vivo stimulation in CD8$^+$ (G) and CD4$^+$ (H) T cells in LKR13 (left) and 368T1 (right) tumors on day 22 after tumor initiation (n = 4 mice per group). Significance was determined using a two-tailed Student's t test (D) or one-way ANOVA (E–H). *P < 0.05, **P < 0.01, ***P < 0.001, ****P < 0.0001, n.s., not significant.

Msh2 KO lung tumors develop acquired resistance to ICIs

LKR13-H tumors chronically treated with anti-PD-1 or anti-PD-1 + anti-CTLA-4 initially responded to the ICIs (defined from here onwards as a reduction in tumor volume of at least 30% compared to pre-treatment), but eventually developed AR (Schoenfeld et al., 2021) (Fig. 2, A and B). We collected tumors at a late AR timepoint (day 39) when tumors had an increase in volume of at least 20% (of note, an increase in the sum of the longest diameters of ≥20% would be considered progressive disease as per RECIST v1.1 criteria in patients) (Schoenfeld et al., 2021). We also defined an early AR timepoint (day 26) when tumors had an increase in volume of any magnitude. To exclude the possibility that the generation of anti-drug antibodies (Kverneland et al., 2018) could result in tumor outgrowth during chronic treatment, we isolated tumors that had developed AR to anti-PD-1 or anti-PD-1 + anti-CTLA-4 and subcutaneously transplanted either dissociated CD45$^-$ cancer (and stromal) cells or ∼2 mm^3 tumor pieces into new recipient mice, which then received anti-PD-1 or anti-PD-1 + anti-CTLA-4 once their tumors reached an average volume of 30–50 mm^3 (Fig. 2 C). Mice implanted with either AR tumor pieces (which maintained the tumor's tissue organization and microenvironment) or dissociated AR cancer cells did not respond to ICI therapy, confirming the resistance phenotype and suggesting that resistance was cancer cell–intrinsic in this setting (Fig. 2 D).

We performed WES in isotype (Iso) control and ICI-resistant LKR13-H tumors to determine whether resistant tumors gained genomic alterations that have been implicated in the development of AR to ICIs in cancer patients (Fig. S1 F). We did not identify genomic alterations in genes related to antigen processing and presentation (*B2m*), IFNγ signaling (*Ifngr1*, *Ifngr2*, *Jak1*, *Jak2*, *Stat1*), or tumor-intrinsic immune suppressive pathways (*Pten*). AR tumors had a greater number of non-synonymous SNVs compared to Iso treated tumors, possibly because they were collected at a later time-point after engraftment: day 39 versus day 16 for Iso.

Resistant tumors harbor dysfunctional tumor-infiltrating lymphocytes (TILs)

Because we did not identify genomic alterations that have been clinically associated with AR to ICIs (although this does not preclude the possibility that novel mutations may contribute to resistance), we focused on transcriptional changes that could be associated with resistance. We performed single-cell RNA sequencing (scRNAseq) on LKR13-H tumors treated with Iso or treated with either anti-PD-1 (P) or anti-PD-1 + anti-CTLA-4 (P+C) that were responding or had developed (late) AR to therapy. Because Iso and responding tumors were highly infiltrated by immune cells, whereas AR tumors were poorly immune-infiltrated and harbored a greater proportion of CD45$^-$ cancer (and stromal) cells (native cell frequencies shown in Fig. 3 A), we pooled cells at a normalized 2:1:1 ratio of T cells, other immune cells, and cancer (and stromal) cells across all treatment groups prior to sequencing. Globally, AR tumor cells clustered separately from Iso and responding cells regardless of treatment (anti-PD-1 or anti-PD-1 + anti-CTLA-4) across clusters of lymphocytes, myeloid cells, and cancer cells identified by lineage marker genes, and <1.5% of cells were identified as stromal or endothelial cells (Fig. S2, A and B).

Within the sub-clustered lymphocyte compartment (Fig. 3 B), we identified 15 clusters of CD8$^+$ T cells and 5 clusters of CD4$^+$ T cells, of which 2 were Foxp3$^+$ regulatory T cells (Tregs) that were enriched in AR tumors (Fig. S2, C–E). We also identified three clusters of *Ncr1*$^+$ NK and *Tcrg-C4*$^+$ γ/δT cells, which were enriched in Iso and responding tumors (Fig. S2, D and E). We focused on the *Cd8*$^+$ and *Cd4*$^+$ *Foxp3*$^-$ TILs from Iso, responding, and AR tumors (Fig. 3 C). T cells from both AR (predominantly in clusters 2 and 14) and Iso and responding tumors (predominantly in cluster 3) expressed naïve and migratory T cell genes (e.g., *Sell*, *S1pr1*). Similarly, expression of proliferative genes (e.g., *Mki67*) was found in both AR (predominantly in cluster 13) and Iso and responding TILs (predominantly in clusters 10 and 16). In contrast, genes related to T cell effector functions including cytotoxicity (e.g., *Gzma*, *Prf1*), cytokine secretion (e.g., *Tnf*, *Il2*, *Ifng*), T cell receptor activation (e.g., *Nr4a1*), and chemokine secretion (e.g., *Cxcl10*) were predominantly expressed by Iso and responding TILs (clusters 9, 15, 8, 12). Cluster 9 expressed the broadest range of genes related to effector T cell function and contained the lowest frequency of AR TILs. However, genes related to T cell exhaustion (e.g., *Pdcd1*, *Lag3*) were also expressed by Iso and responding TILs (predominantly in clusters 22, 0, 4, and 6), indicating that even in tumors responding to therapy a significant proportion of TILs lacked effector functions and expressed markers of T cell exhaustion. AR TILs (predominantly in clusters 18 and 21) also expressed exhaustion genes. Cluster 21, derived almost entirely from AR to anti-PD-1 cells, showed particularly elevated expression of transcription factors associated with T cell exhaustion, *Eomes* and *Tox*.

Immunophenotyping via flow cytometry validated these results, demonstrating a decrease in TILs both at early (day 26) and late (day 39) AR timepoints compared to TILs in tumors responding to anti-PD-1 (Fig. 3 D). In tumors treated with anti-PD-1 + anti-CTLA-4, we found a significant decrease in the number of CD4$^+$ TILs and a trend toward decreasing CD8$^+$ TILs in AR tumors (Fig. 3 D). Similarly, IFNγ production after ex vivo stimulation was higher in TILs isolated from responding tumors than from early and late AR tumors (Fig. 3 E). Treg abundance was also increased in early and late AR tumors (Fig. 3 F). Collectively, tumors with AR to ICIs harbored fewer TILs

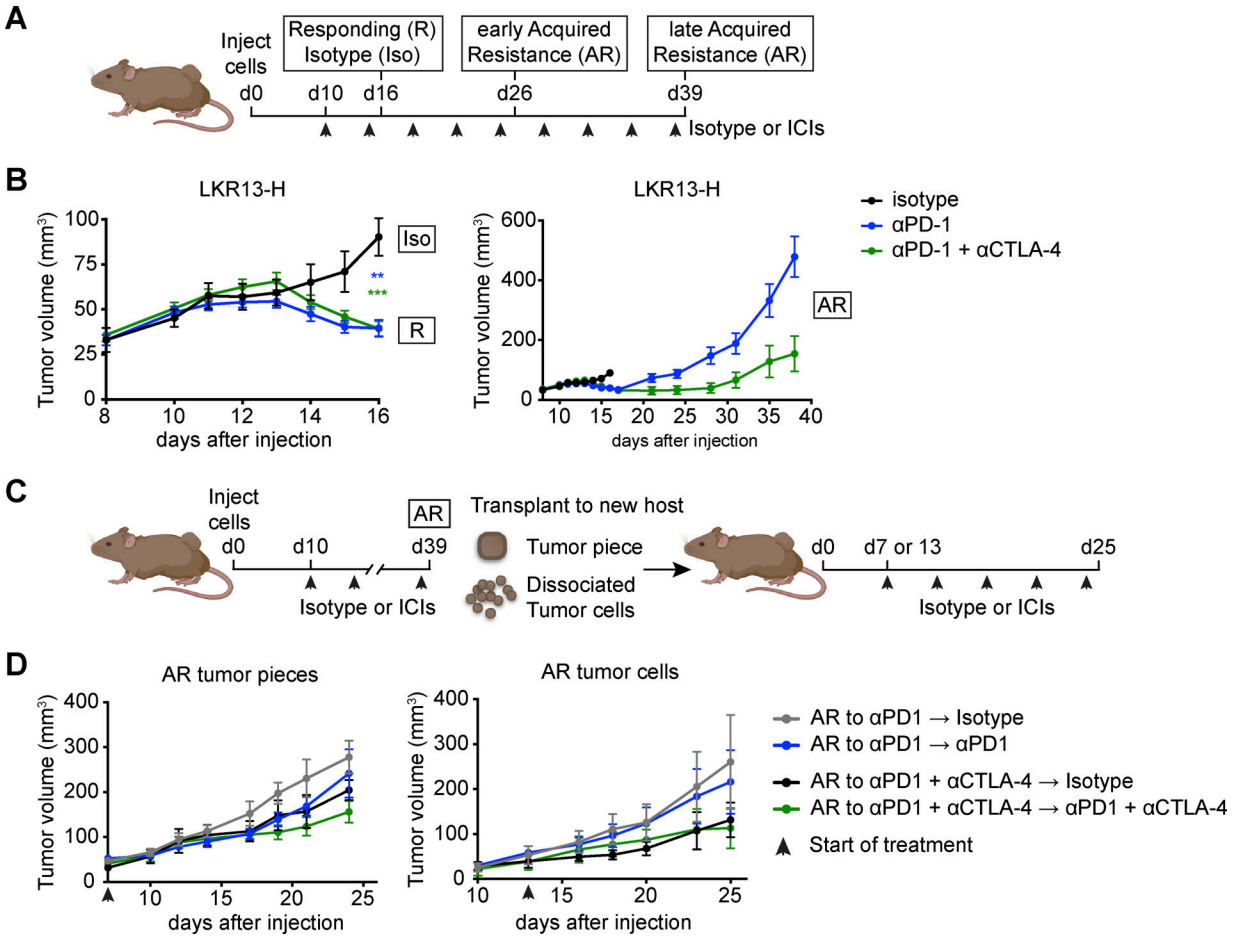

Figure 2. ***Msh2* KO LKR13-H tumors develop acquired resistance to ICIs. (A)** Experimental strategy for induction of acquired resistance: 500,000 LKR13-H cells were injected subcutaneously into syngeneic B6129SF1/J mice treated with either Iso, anti-PD-1 (P), or anti-PD-1 + anti-CTLA-4 (P+C) twice weekly starting on day (d) 10. Tumors were collected on day 16 from mice that received Iso or were responding (R) to therapy. Tumors from mice that developed AR to therapy were collected on day 26 (early AR) or day 39 (late AR). **(B)** LKR13-H tumor growth curves up to day 16 (left) or day 39 (right; note different axis scales). A cohort of mice was treated until day 16 (n = 6 mice per group) and the remaining mice were treated until day 39 (n = 6 mice per group; data shown are representative of at least two independent experiments). **(C)** Experimental strategy for transplantation of resistant tumors: LKR13-H tumors that developed acquired resistance to either anti-PD-1 or anti-PD-1 + anti-CTLA-4 (n = 3 mice per group) were collected on day 39. Half the tumor volume was dissociated and the $CD45^-$ cancer (and stromal) cell fraction was isolated via FACS, whereas the remaining half of the tumor was dissected into ∼2 mm^3 pieces. The tumor pieces and dissociated cancer (and stromal) cells were subcutaneously implanted into syngeneic B6129SF1/J mice and treated with either Iso, anti-PD-1, or anti-PD-1 + anti-CTLA-4 on day 7 (tumor pieces; n = 3–4 mice per group) or day 13 (dissociated cells, n = 2–3 mice per group). **(D)** Tumor growth curves for tumor pieces (left) and dissociated cells (right) isolated from resistant tumors and transplanted into new syngeneic hosts; no significant difference in final tumor volumes was found between isotype and ICI-treated groups. Analyses were performed using two-tailed Student's t test (B and D). **P < 0.01, ***P < 0.001.

compared to responding tumors, and AR TILs were characterized by impaired effector function and expression of T cell exhaustion genes.

After sub-clustering myeloid cells (Fig. S2 F, top) from the full scRNAseq dataset (Fig. S2 A), we identified five dendritic cell (DC) and eight monocyte/macrophage clusters (Fig. S2 F, bottom). Although three of five DC clusters contained cells predominantly from Iso and responding tumors, DC cluster 18 expressed genes related to tissue residency and cDC1 differentiation (*Itgae*, *Xcr1*, *Irf8*) and contained cells from both responding and AR tumors, suggesting that these cells were not depleted from resistant tumors. However, monocyte/macrophage clusters defined by elevated expression of chemokines *Cxcl9* (cluster 6) or *Cxcl10* (cluster 9) contained cells predominantly from Iso and responding tumors; decreased expression of these chemokines may contribute to T cell exclusion from AR tumors (Fig. S2 F).

Resistant cancer cells lose MHC-II expression despite intact IFNγ responses

To investigate whether cancer cell–intrinsic mechanisms contributed to the exclusion of TILs at resistance, we analyzed differentially expressed genes (DEGs) in cancer cells (*Krt8+* and *Krt18+*; Fig. S2 B) in the scRNAseq dataset (Fig. 4 A and Fig. S3 A) and performed gene-set enrichment analysis (GSEA) (Table S1). Of note, the Gene Ontology (GO) Antigen Processing & Presentation gene set was significantly enriched (false discovery rate [FDR] q value <0.25; P value <0.05) in cancer cells responding to

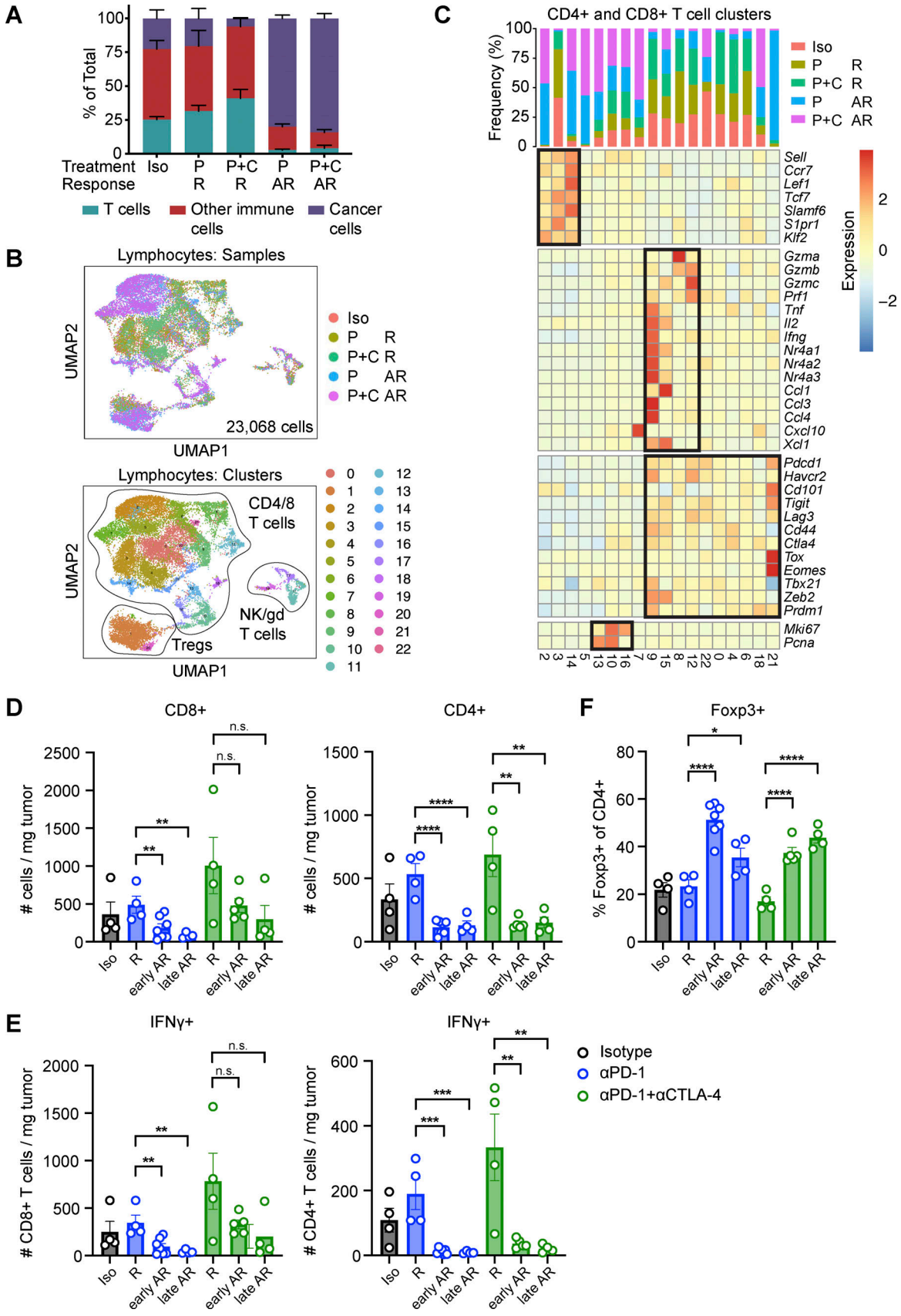

Figure 3. **Decreased immune infiltration and dysfunctional TILs in tumors with AR to ICIs. (A–C)** LKR13-H tumors were collected from B6129SF1/J mice that received Iso and mice that were responding (R) to either anti-PD-1 (P) or anti-PD-1 + anti-CTLA-4 (P+C) therapy on day 16. Tumors were collected from

mice that developed AR to therapy on day 39 (late AR). **(A)** The percentage of CD4+ and CD8+ T cells, CD45+ CD4/8$^-$ other immune cells, and CD45$^-$ cancer (and stromal) cells isolated via FACS from LKR13-H tumors (n = 3 mice per group). **(B)** UMAP projection showing lymphocytes from LKR13-H tumors in A colored by treatment condition (top) and cluster (bottom). NK, natural killer. **(C)** Percentage of cells by treatment condition (top) and heatmap showing mean expression of selected genes (bottom) in CD4/8$^+$ T cell clusters from B. **(D–F)** LKR13-H tumors were collected from mice that received Iso and mice that were responding (R) to either anti-PD-1 (P) or anti-PD-1 + anti-CTLA-4 (P+C) therapy on day 16. Tumors were collected from mice that developed AR to therapy either on day 26 (early AR) or day 39 (late AR). Number of CD8$^+$ (left) and CD4$^+$ (right) T cells (D), number of CD8$^+$ (left) and CD4$^+$ (right) T cells producing IFNγ after ex vivo stimulation (E), and number of Foxp3$^+$ Tregs (F) in LKR13-H tumors (n = 4–7 mice per group). Significance was determined using one-way ANOVA (D–F). *P < 0.05, **P < 0.01, ***P < 0.001, ****P < 0.0001, n.s., not significant.

ICIs, whereas the Hallmark Hypoxia gene set was significantly enriched (FDR q value <0.25; P value <0.05) in cancer cells with AR (Fig. S3, B and C).

Surprisingly, the expression of MHC-I (*H2-D1*, *H2-K1*), *Tap1*, and *Tap2* was only slightly reduced in AR cancer cells, yet the expression of MHC-II (*H2-Aa*, *H2-Ab1*) and the MHC-II chaperone *Cd74* was markedly reduced (Fig. 4 B). MHC-II can be induced by IFNγ, and although constitutively expressed genes in the IFNγ signaling pathway (e.g., *Ifngr1, Jak1)* were expressed at similar levels in Iso, responding, and AR cancer cells, IFN-inducible genes (e.g., *Stat1*, *Irf1*) were markedly decreased in these cells. Importantly, the MHC-II transactivator, *Ciita*, was also reduced in AR cancer cells (Fig. 4 B). Validating these findings, CD45$^-$ cancer (and stromal) cells from AR tumors, either at an early (day 26) or late (day 39) resistance timepoint, had significantly reduced cell surface MHC-II and MHC-I levels compared to responding tumors (Fig. 4 C), and cell surface PD-L1 was similarly reduced (Fig. S3 D).

Based on this unexpected cancer cell–intrinsic MHC-II expression, we next tested whether CD4$^+$ T cells were required for response to ICIs. Depletion of CD4$^+$ T cells alone (or CD8$^+$ T cells alone) abrogated the response to ICIs in LKR13-H tumors, consistent with prior co-depletion results (Fig. 4 D and Fig. S3 E). Neutralizing IFNγ also abrogated the response to ICIs (Fig. 4 D). Both CD4$^+$ T cell depletion and IFNγ neutralization, but not CD8$^+$ T cell depletion, resulted in decreased MHC-I and MHC-II expression in CD45$^-$ cancer (and stromal) cells, further highlighting the role of IFNγ in driving cancer cell–intrinsic MHC expression in vivo (Fig. 4 E). To distinguish between decreased availability of IFNγ in the tumor microenvironment (TME) versus cancer cell–intrinsic defects in IFN signaling as drivers of MHC-II loss in resistant cancer cells, we generated two cell lines from LKR13-H tumors with AR to anti-PD-1 (PAR60, PAR74) and two cell lines from tumors with AR to anti-PD-1 + anti-CTLA-4 (PCAR15, PCAR24). Upon in vitro exposure to IFNγ, PAR and PCAR cell lines retained the capacity to induce MHC-II, MHC-I, and PD-L1, indicating that IFN signaling was not impaired in AR cancer cells (Fig. 4 F and Fig. S3 F). Collectively, these results suggest that loss of MHC-II in resistant cancer cells is a consequence of decreased IFNγ availability in the TME, partly caused by T cell exclusion and dysfunction.

Despite their similar levels of IFNγ-induced surface MHC expression, we investigated whether there was a difference in the abundance of peptide antigens presented by AR cancer cells compared to control LKR13-H cells. Using mass spectrometry (MS), we identified a decrease in the abundance of peptides presented by MHC molecules in resistant cancer cells (Fig. S4, A–D). We identified approximately half as many MHC-I (H2-K^b and H2-D^b) and MHC-II (H2-IA^b) restricted peptides from PCAR15 and PCAR24 cells compared to LKR13-H cells (Fig. S4, C and D). Using the MhcVizPipe workflow (Kovalchik et al., 2022), the binding affinity of eluted 8–12-mer peptides to H2-K^b and H2-D^b, and of 9–22-mer peptides to H2-IA^b, was predicted with NetMHCpan (Fig. S4, E and F top). Unsupervised GibbsCluster analysis was performed to identify MHC-I and MHC-II peptide binding motifs, and these were similar across the three cell lines (Fig. S4, E and F bottom). Although the mixed background of the cell lines precluded us from definitively identifying neoantigens, these results suggest that resistant PCAR15 and PCAR24 cells presented fewer total peptides.

Hypoxia in resistant tumors is associated with decreased cancer cell–intrinsic MHC-II and TIL exclusion

Tumor hypoxia is associated with poor outcomes across diverse cancer types and contributes to primary resistance to ICIs, partly by promoting immunologically "cold" or "excluded" TMEs with poor T cell infiltration (Vaupel and Mayer, 2007; Barsoum et al., 2014). GSEA of cancer cell clusters indicated that the Hallmark Hypoxia gene set was enriched in tumors resistant to ICIs (Fig. S3 C), and over half of the enriched hypoxia genes were related to glycolysis, including *Slc2a1* (which encodes the glucose transporter Glut1) and several glycolytic enzymes (Fig. 5 A; additional glycolytic enzymes and hypoxia-related genes are shown in Fig. S5 A). We also identified a cluster of macrophages with elevated expression of glycolysis-related genes that were derived almost exclusively from AR tumors (Fig. S2 F). To validate these results, we measured glucose uptake and hypoxia in ICI-treated tumors. CD45$^-$ cancer (and stromal) cells from both early and late AR tumors had increased hypoxia detected by pimonidazole staining via flow cytometry (Fig. 5 B). Importantly, early AR tumors (particularly those treated with anti-PD-1 + anti-CTLA-4) were not significantly larger than isotype-treated control tumors, indicating that the elevated hypoxia was not simply attributable to differences in tumor size (Fig. S5 B). Pimonidazole staining by immunofluorescence (Fig. 5, C–E) also showed that late AR tumors had increased hypoxia, quantified by fields of view (FOV) (Fig. 5 C) or per tumor (Fig. S5 C). Confirming the link between hypoxia and glycolysis, CD45$^-$ cancer (and stromal) cells from AR tumors (with the exception of early AR to anti-PD1 tumors) had increased uptake of the fluorescent glucose analog 2-NBDG compared to responding tumors, suggesting increased glycolytic potential (Fig. 5 F).

For FOV in which a hypoxic region was detected and contained at least 10 cells, we compared the abundance of CD3$^+$ T cells in hypoxic versus normoxic tumor regions of that same FOV. T cells were significantly reduced in hypoxic regions of

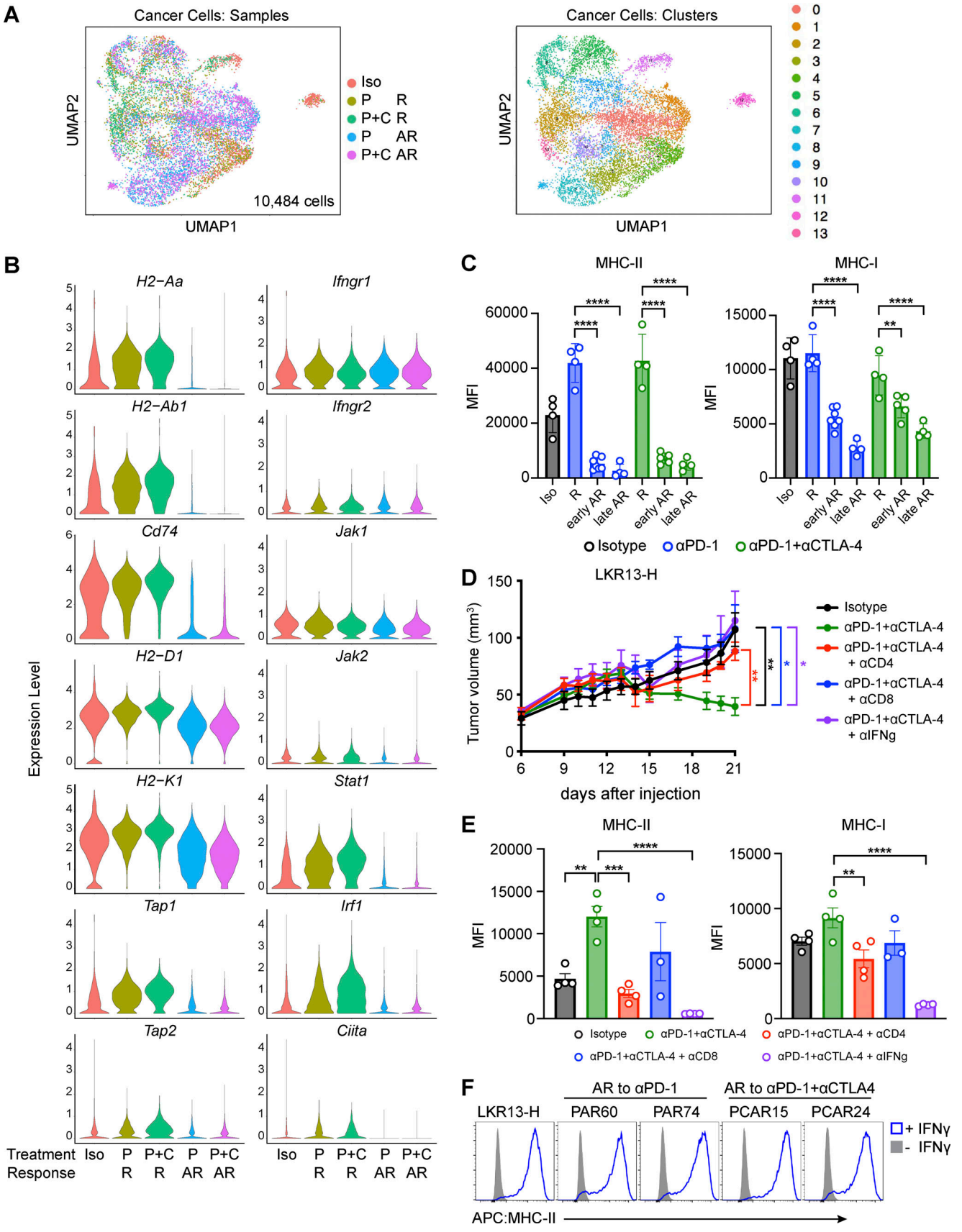

Figure 4. **Loss of cancer cell–intrinsic MHC class II expression in tumors with acquired resistance is not driven by defects in IFNγ signaling. (A)** UMAP projection of cancer cells from LKR13-H tumors colored by treatment condition (left) and cluster (right). **(B)** Violin plots showing expression levels of selected

genes in cancer cells from A by treatment condition. **(C)** Surface expression of MHC-II (left) and MHC-I (right) in CD45⁻ cancer (and stromal) cells isolated from LKR13-H tumors collected from isotype-treated B6129SF1/J mice (Iso) and mice that were responding (R) to either anti-PD-1 (P) or anti-PD-1 + anti-CTLA-4 (P+C) therapy on day 16, and mice that developed AR to therapy either on day 26 (early AR) or day 39 (late AR) (n = 4–7 mice per group). **(D)** LKR13-H tumors were treated with isotype or anti-PD-1 + anti-CTLA-4 and with either anti-CD4, anti-CD8, or anti-IFNγ antibodies twice weekly starting on day 10 (n = 4 mice per group). **(E)** Surface expression of MHC-II (left) and MHC-I (right) in CD45⁻ cancer (and stromal) cells isolated from tumors shown in D collected on day 22 (n = 3–4 mice per group). **(F)** Expression of MHC-II after in vitro IFNγ stimulation in LKR13-H cells and four cell lines derived from LKR13-H tumors that developed acquired resistance to either anti-PD-1 (PAR60, PAR74) or anti-PD-1 and anti-CTLA-4 (PCAR15, PCAR24). Significance was determined using one-way ANOVA (C and E) or two-tailed Student's t test (D). *P < 0.05, **P < 0.01, ***P < 0.001, ****P < 0.0001.

tumors responding to ICIs. Similarly, T cells were significantly reduced in hypoxic regions of tumors resistant to anti-PD-1 + anti-CTLA-4, and a trend towards a decrease was seen in tumors resistant to anti-PD1 alone (Fig. 5 E). Immunofluorescence staining also showed that the overall abundance of T cells was decreased in AR tumors (Fig. S5 D).

Because hypoxia can cell-intrinsically modulate cancer cell MHC-I expression (Murthy et al., 2019; Marijt et al., 2019), we tested whether hypoxia could similarly impact MHC-II expression in LKR13 cells exposed to IFNγ under normoxic (21% O_2) or hypoxic (1% O_2) conditions in vitro. Although IFNγ-induced MHC-I expression was not affected by hypoxia, MHC-II induction was impaired under hypoxic conditions in (*Msh2* WT) LKR13-EV cells, (*Msh2* KO) LKR13-H cells, and two cell lines derived from ICI-resistant LKR13-H tumors (PCAR15, PCAR24) (Fig. 5 G and Fig. S5 E).

Together, these results suggest that increased hypoxia in resistant tumors can contribute to impaired cancer cell MHC-II expression not only through T cell exclusion and reduced T cell–derived IFNγ but also through cancer cell–intrinsic mechanisms.

Hypoxia correlates with worse outcomes in NSCLC patients treated with ICIs

Because hypoxia emerged as a dominant feature of tumors that developed AR, we generated a hypoxia metagene signature from the LKR13-H scRNAseq data (see Materials and methods) and correlated its expression with lung cancer patient outcomes following immune checkpoint inhibition in 152 whole transcriptome RNAseq specimens from the Stand Up To Cancer–Mark Foundation (SU2C-MARK) cohort, collected prior to ICI treatment (Ravi et al., 2023). The majority of these patients were treated with PD-1/PD-L1 inhibitors alone, although a subset received PD-1/PD-L1 inhibitors in combination with CTLA-4. Response to checkpoint inhibitors in this cohort correlated with nonsynonymous TMB (Rizvi et al., 2015) and an exhausted CD8⁺ T cell signature (Sade-Feldman et al., 2018), in line with prior studies. We first assessed the expression of the hypoxia metagene across three response categories quantified using RECIST v1.1 criteria: partial response or complete response (PR/CR), stable disease (SD), or progressive disease (PD), and we found that higher hypoxia metagene expression was associated with PD (Fig. 6 A). Moreover, high hypoxia metagene expression was strongly associated with decreased progression-free survival (P < 0.005, log-rank test; Fig. 6 B).

Combination treatment with anti-hypoxia agent TH-302 and ICIs extends the benefits of ICI therapy

To test whether reducing tumor hypoxia could delay AR, we used TH-302, a hypoxia-activated pro-drug that is active under low oxygen tension and cytotoxic to proliferating cells (Meng et al., 2012; Duan et al., 2008). Mice bearing LKR13-H tumors were treated with Iso, anti-PD-1 + anti-CTLA-4, TH-302, or ICIs plus TH-302 starting on day 10 after tumor initiation (Fig. 6 C). After 10 days of treatment, TH-302 alone did not significantly impact tumor burden compared to Iso, and the addition of TH-302 to ICIs did not impact response to ICIs at this early timepoint (Fig. 6 D, left). Consistent with these results, the abundance and cytokine production of CD8⁺ and CD4⁺ T cells were generally not impacted by TH-302 treatment at day 16, although anti-PD-1 + anti-CTLA-4 either alone or in combination with TH-302 reduced the abundance of Foxp3⁺ Tregs (Fig. S5, F–H). LKR13-H tumors eventually developed AR during chronic treatment with ICIs, but the combination of TH-302 and ICIs significantly delayed the emergence of AR (Fig. 6 D, right). TH-302 alone also increased MHC-II expression on CD45⁻ cancer (and stromal) cells, further supporting a role for hypoxia in cell-intrinsically modulating MHC-II in vivo (Fig. S5 I). Tumors that developed AR to the combination of ICI + TH-302 had increased expression levels of anti-apoptotic protein Bcl-2, but not senescence-associated protein HMGB1 (Fig. S5, J–L). Pimonidazole immunofluorescence staining quantified using QuPath confirmed that TH-302 reduced hypoxic tumor areas (Fig. 6, E and F; and Fig. S5 M).

Discussion

To identify novel drivers of AR to ICIs in lung cancer, we investigated the genomic, transcriptional, and functional features of *Msh2* KO tumors that initially responded but eventually developed AR to anti-PD-1 alone or anti-PD-1 plus anti-CTLA-4. We found that resistant tumors were characterized by elevated hypoxia, decreased TILs, decreased cancer-cell intrinsic MHC-I, and most strikingly, MHC-II. Hypoxia was also associated with worse outcomes on ICIs in lung cancer. Targeting hypoxic tumor regions with TH-302, a hypoxia-activated cytotoxic agent, delayed AR to therapy.

Consistent with prior studies of tumors with genetically engineered MMRd (Germano et al., 2017; Mandal et al., 2019; Martinez-Usatorre et al., 2021; Westcott et al., 2023), we found that *Msh2* deletion in two $Kras^{G12D}$-driven lung adenocarcinoma cell lines from distinct mouse models ($p53^{WT}$ LKR13 [Wislez et al., 2005; Johnson et al., 2001] and $p53^{flox/flox}$ 368T1 [Winslow et al., 2011; DuPage et al., 2009]) led to the accumulation of somatic mutations and resulted in an elevated TMB (Fig. 1 B). Subcutaneous *Msh2* KO LKR13-L and LKR13-H tumors responded to ICIs, consistent with findings in B16F10 and CT26 models (Mandal et al., 2019). Yet *Msh2* KO 368T1-L and 368T1-H

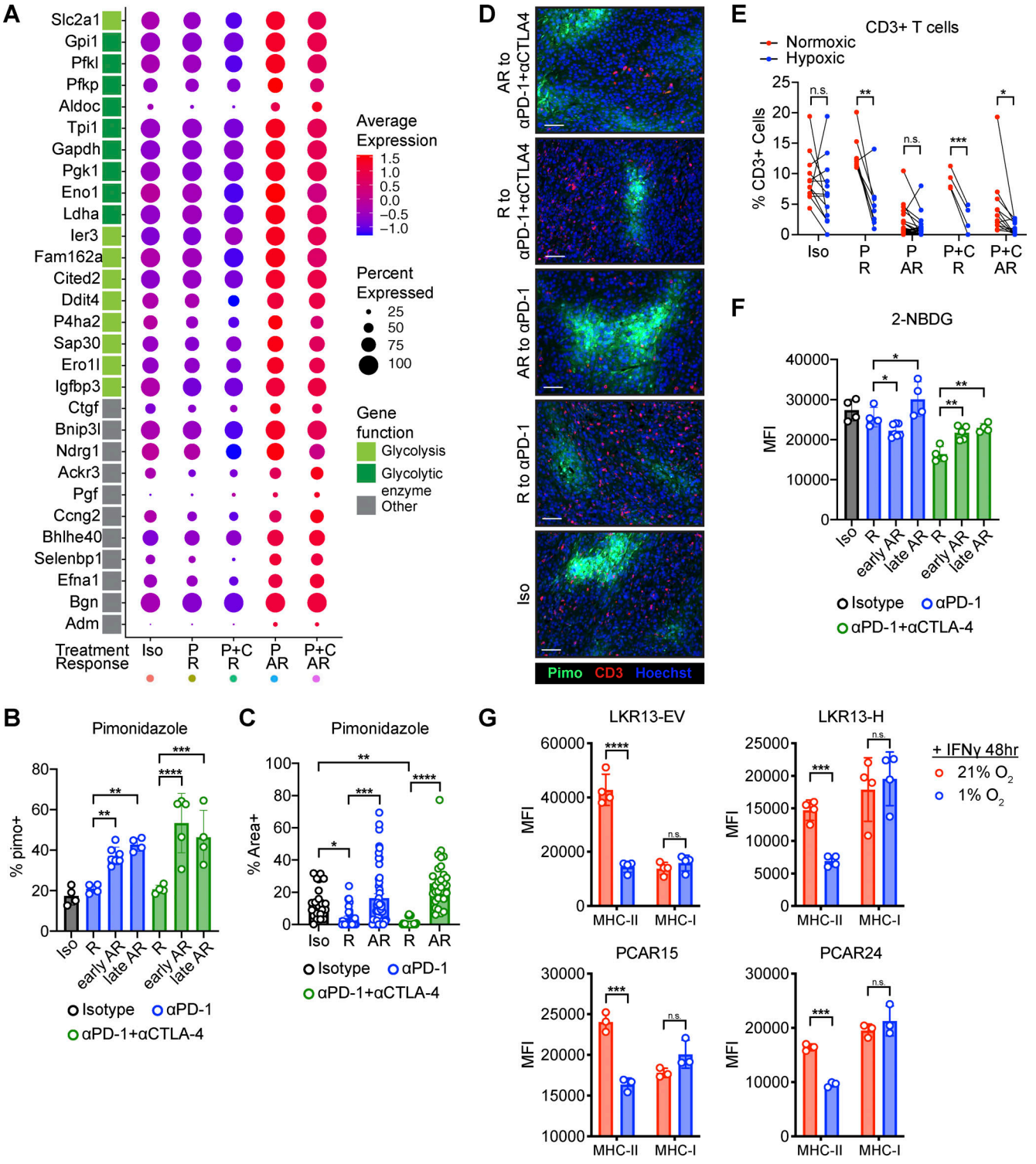

Figure 5. **Hypoxia in acquired resistant tumors is associated with decreased cancer cell–intrinsic MHC-II and TIL exclusion. (A)** Dotplot showing the cancer cell expression of Hallmark Hypoxia genes enriched in tumors with AR to either anti-PD-1 or anti-PD-1 + anti-CTLA-4 by treatment condition. **(B)** Expression of hypoxia marker pimonidazole in CD45⁻ cancer (and stromal) cells from LKR13-H tumors collected from isotype-treated B6129SF1/J mice (Iso) and mice that were responding (R) to either anti-PD-1 (P) or anti-PD-1 + anti-CTLA-4 (P+C) therapy on day 16, and mice that developed AR to therapy either on day 26 (early AR) or day 39 (late AR) (n = 4–7 mice per group). **(C–E)** Immunofluorescence staining for pimonidazole (FITC, green) and CD3 (Alexa Fluor 594, red) in LKR13-H tumors collected from mice treated with Iso and mice that were responding (R) to either anti-PD-1 (P) or anti-PD-1 + anti-CTLA-4 (P+C) therapy on day 16 and mice that developed AR to therapy on day 39 (n = 3 mice per group). DNA was stained with Hoechst (blue). **(C)** Percent hypoxic (pimonidazole+) area quantified using QuPath from at least six FOV per tumor. **(D)** Immunofluorescence images representative of the average percent hypoxic area in each treatment group. Scale bars, 50 µm. **(E)** Percentage of CD3⁺ T cells quantified using QuPath in pimonidazole+ hypoxic areas and pimonidazole- normoxic areas for each FOV from C in which hypoxia was detected. **(F)** Uptake of glucose analog 2-NBDG in CD45⁻ cancer (and stromal) cells from LKR13-H tumors

collected as in B. **(G)** Surface expression of MHC-II and MHC-I after 48 h in vitro IFNγ stimulation under 21% oxygen (normoxia) or 1% oxygen (hypoxia) in *Msh2* WT LKR13-EV cells, *Msh2* KO LKR13-H cells, and two cell lines derived from LKR13-H tumors that developed acquired resistance to anti-PD-1 and anti-CTLA-4 (PCAR15, PCAR24). *n* = 3–4 technical replicates, representative of two (PCAR15, PCAR24) or four (LKR13-EV, LKR13-H) independent experiments. Significance was determined using one-way ANOVA (B, C, and F), paired two-tailed Student's *t* test (E), or unpaired two-tailed Student's *t* test (G). *P < 0.05, **P < 0.01, ***P < 0.001, ****P < 0.0001, n.s., not significant. MFI, mean fluorescence intensity.

tumors, which are p53 deficient, did not respond to ICIs despite harboring similar numbers of non-synonymous SNVs as the LKR13 tumors (Fig. 1 D). Although these results could suggest that p53 deficiency may contribute to the lack of response to ICIs in the *Msh2* KO 368T1 tumors, immunogenic and isogenic lung cancer models which differ only in their p53 mutational status would be required to investigate this possibility. Yet 368T1 and LKR13 cells differ in other important ways: (1) they are derived from distinct murine models ($Kras^{LSL\text{-}G12D/+}$; $p53^{flox/flox}$ versus $Kras^{LA1}$, respectively) and (2) the *Msh2* KO lines each harbor unique non-synonymous mutations, despite similar overall TMBs. In the clinic, median TMBs and response rates to PD-1 pathway inhibitors are similar or higher in patients with *KRAS*-mutant lung adenocarcinomas harboring *TP53* mutations

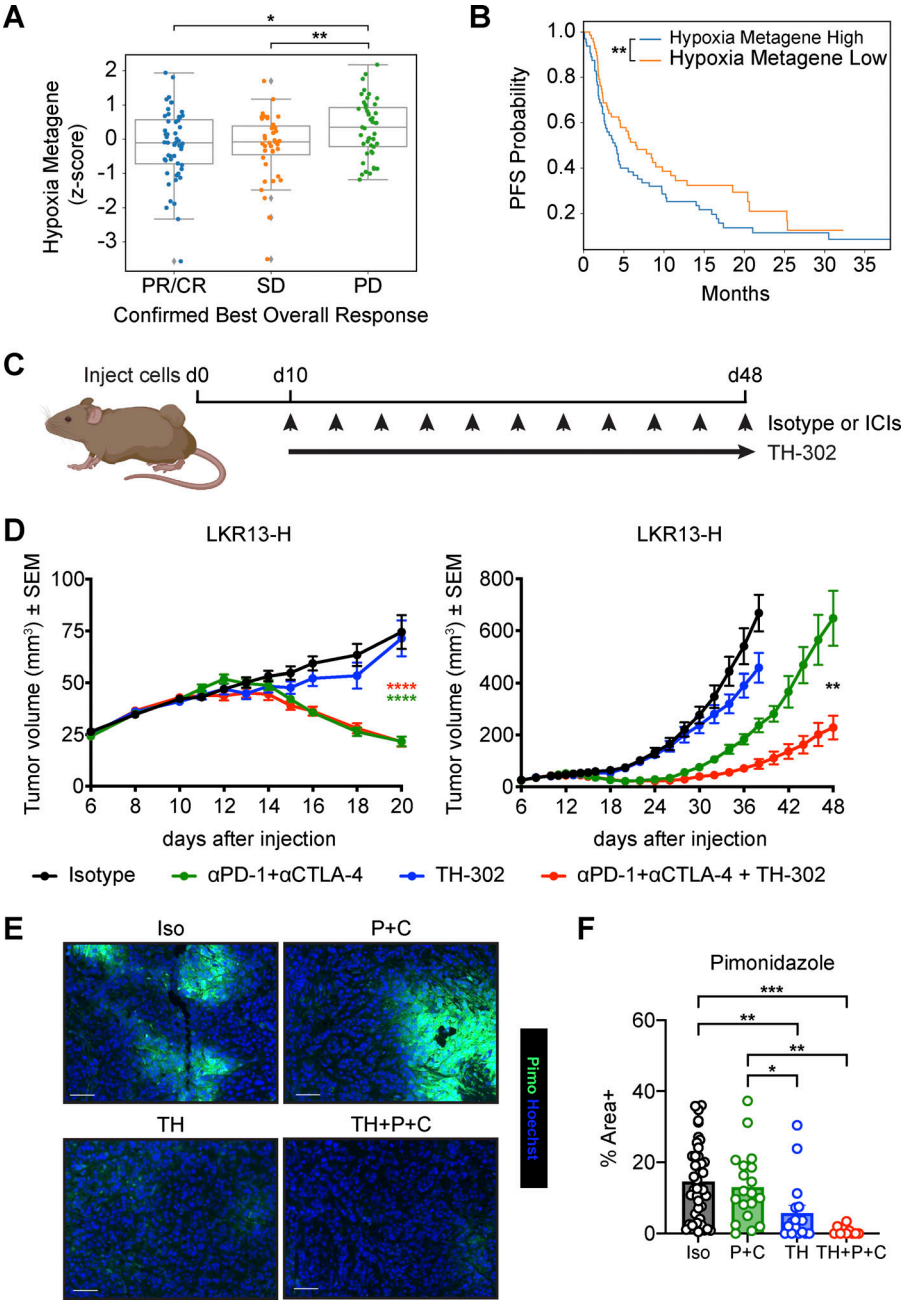

Figure 6. **Hypoxia ablation extends the benefits of anti-PD-1 + anti-CTLA-4 therapy in *Msh2* KO LKR13-H tumors. (A)** Hypoxia metagene expression (z-score) as a function of response category: complete response (CR), partial response (PR), stable disease (SD), progressive disease (PD). **(B)** Kaplan–Meier curves for progression-free survival (PFS) in patients with high (top 50%, *n* = 72) or low (bottom 50%, *n* = 71) hypoxia metagene expression. **(C)** Experimental strategy: B6129SF1/J mice bearing subcutaneous LKR13-H tumors were treated with either Iso or anti-PD-1 + anti-CTLA-4 twice weekly and/or with TH-302 every other day starting on day 10 after tumor initiation. **(D)** LKR13-H tumor growth curves up to day 20 (left) or day 48 (right; note different axis scales). Data shown are a collection of three independent experiments with 3–5 mice per group (total 12–14 mice per group). **(E and F)** Immunofluorescence staining for pimonidazole (FITC, green) in LKR13-H tumors collected from mice treated with Iso or anti-PD-1 + anti-CTLA-4 and/or with TH-302 (*n* = 3–4 mice per group). DNA was stained with Hoechst (blue). **(E)** Immunofluorescence images are representative of the average percent hypoxic area in each treatment group. Scale bars, 50 µm. **(F)** Percent hypoxic (pimonidazole+) area quantified using QuPath from at least three FOV per mouse. Significance was determined using Mann–Whitney *U* test (A), log-rank test (B), two-tailed Student's *t* test (D) or one-way ANOVA (F). *P < 0.05, **P < 0.01, ***P < 0.001.

compared to those with *TP53*-WT tumors (Skoulidis et al., 2018), further suggesting that p53 deficiency is not the only mediator of primary ICI resistance in the *Msh2* KO 368T1 tumors. Indeed, in autochthonous $Kras^{G12D}$-driven and p53-deficient lung tumors, *Msh2* deletion or *APOBEC3B* expression increased TMB but did not sensitize tumors to ICIs (although some cell lines derived from these models with even higher TMB than the original tumors were sensitive) (Martinez-Usatorre et al., 2021; Westcott et al., 2023; Boumelha et al., 2022). These studies along with others (Wolf et al., 2019; Gejman et al., 2018; McGranahan et al., 2016) indicate that mutational intra-tumoral heterogeneity (ITH) likely affects tumor immunogenicity and sensitivity to ICIs. In our study, both ICI-sensitive LKR13-L and LKR13-H tumors and ICI-insensitive 368T1-L and 368T1-H tumors were clonal, suggesting that additional features beyond TMB and ITH can shape sensitivity to ICIs.

Unexpectedly, tumors responding to ICIs expressed high levels of cancer cell–intrinsic MHC-II, whereas resistant cancer cells did not (Fig. 4, B and C). These results are consistent with murine lung cancer studies in which tumor MHC-II expression correlated with response to anti-PD-1 therapy (Johnson et al., 2020). In cancer patients, bulk and cancer cell–specific MHC-II expression correlates with improved clinical outcomes, including after ICIs (Ayers et al., 2017; Cristescu et al., 2018; Axelrod et al., 2019; Datar et al., 2021; Johnson et al., 2016). In NSCLC, cancer cell–specific MHC-II was identified in ∼70–85% of cases, and tumors with reduced tumor-specific MHC-II harbored fewer T cells, a pattern similar to resistant LKR13-H tumors (Datar et al., 2021). Thus, MHC-II expression in LKR13 cells was consistent with the broad expression of cancer cell–intrinsic MHC-II in human lung cancers. We also found that the capacity of LKR13 cancer cells to induce MHC-II, but not MHC-I, after exposure to IFNγ was impaired in a cell-intrinsic manner under hypoxic conditions (Fig. 5 G). Hypoxia has been shown to impair IFNγ-stimulated MHC-I expression in B16F10 and other cancer cells, either alone (Murthy et al., 2019) or in combination with glucose deprivation (Marijt et al., 2019), in part by reducing Stat1 phosphorylation levels (Ivanov et al., 2007; Chandrasekaran et al., 2019). In contrast to these findings, the capacity of LKR13 cells to induce MHC-I (and PD-L1) upon IFNγ stimulation was not impacted, and only MHC-II was affected. Although the specific mechanisms by which hypoxia regulates cancer cell-intrinsic IFNγ-driven MHC-II induction remain to be determined, our results identify a previously unrecognized link between hypoxia and MHC-II expression that warrants further investigation and exemplifies the heterogeneity of responses to hypoxic stress across different cancers.

Solid tumors in which proliferation outpaces the capacity of tumor vasculature, itself often dysregulated (Kerbel, 2008), to provide oxygen to rapidly dividing cells are characterized by gradients of oxygen availability and heterogeneous oxygen consumption (Pouyssegur et al., 2006; Wilson and Hay, 2011). Tumor hypoxia is correlated with poor prognosis and resistance to radio-, chemo-, and immune therapies (Minassian et al., 2019; Walsh et al., 2014; Zandberg et al., 2021) and contributes to the generation of immunosuppressive tumor microenvironments (Barsoum et al., 2014). In a small cohort of melanoma patients with tumors resistant to anti-CTLA-4 therapy who went on to receive anti-PD-1, transcriptional profiling revealed that non-responders to anti-PD-1 treatment had tumors with increased expression of genes associated with hypoxia and glycolysis (Jaiswal et al., 2020). Increased expression of glycolysis-related genes was also correlated with decreased T cell infiltration in melanoma and lung cancer (Cascone et al., 2018). Analysis of transcriptional hypoxia signatures from 19 tumor types using TCGA datasets identified lung squamous carcinomas as among the most hypoxic tumor types, and lung adenocarcinomas had intermediate overall hypoxia but one of the highest levels of intertumoral variability in hypoxia (Bhandari et al., 2019). Similarly, an analysis of human lung tumors using multimodal imaging and intra-operative ^{13}C-glucose infusion found a high degree of inter- and intra-tumoral heterogeneity in glucose utilization, in which less-perfused tumor regions relied more on glucose metabolism and had enhanced expression of genes related to glycolysis as well as oxidative phosphorylation (Hensley et al., 2016). Thus, hypoxia-associated metabolic re-wiring, including increased glucose metabolism, is heterogeneous within lung cancers. This heterogeneity could produce localized hypoxic regions within tumors which may be less responsive to immune therapies.

By contributing not only to a reduction in cancer cell intrinsic MHC-II expression, but also to the exclusion of T cells, hypoxia emerged as a dominant feature of resistant LKR13-H tumors. Interestingly, while AR tumors exhibited an elevated hypoxia signature and increased pimonidazole staining indicative of hypoxia, the transcriptional levels of *Hif1a* itself were reduced. This could be due to negative feedback of its expression and variability in *Hif1a* levels following chronic exposure to hypoxia (Cavadas et al., 2015; Lin et al., 2011). T cells were drastically reduced in resistant tumors compared to tumors responding to ICI therapy (Fig. 3, A, D, and E), and in particular T cells were excluded from hypoxic tumor regions, which were themselves increased in resistant tumors (Fig. 5, B–E). T cell exclusion from hypoxic tumor areas has been identified in a range of murine cancers (Hatfield et al., 2015; Jayaprakash et al., 2018), and diverse methods including treatment with metformin (Scharping et al., 2017; Jaiswal et al., 2020; Park et al., 2021) or TH-302 (Jayaprakash et al., 2018), or genetically inhibiting oxidative metabolism (Najjar et al., 2019) have been employed to reduce tumor hypoxia. Targeting tumor hypoxia resulted in increased sensitivity to ICI treatment in models of melanoma (Scharping et al., 2017; Najjar et al., 2019) colon carcinoma (Scharping et al., 2017), and prostate cancer (Jayaprakash et al., 2018). However, in a model of AR to combination immunotherapy (including anti-PD-1 and anti-CTLA-4) generated by serial in vivo passage of B16 melanoma tumors, tumor hypoxia reduction via metformin treatment failed to sensitize mice to immunotherapy (Jaiswal et al., 2020). In addition, targeting glycolysis with either 2-Deoxy-D-glucose (a glucose structural analog) or the LDH-A inhibitor GSK2837808A also failed to sensitize resistant tumors to immunotherapy (Jaiswal et al., 2020). These results suggest that, once immunotherapy-resistant tumors acquired a hypermetabolic phenotype characterized by increased hypoxia, glycolysis, and oxidative phosphorylation, targeting these pathways

pharmacologically was insufficient to reverse the resistance phenotype.

Based on these findings, we hypothesized that combating AR to ICIs in LKR13-H tumors would require targeting tumor hypoxia before resistance to immunotherapy emerged, with the goal of preventing or delaying resistance rather than overcoming an established resistant state. Thus, rather than waiting for the outgrowth of ICI-resistant tumors and testing additional combination therapies in resistant tumors, we evaluated the impact of adding the hypoxia-activated cytotoxic agent, TH-302, to combination anti-PD-1 plus anti-CTLA-4 treatment from the initiation of therapy on day 10 after tumor engraftment. Although LKR13-H tumor regression upon treatment with anti-PD-1 and anti-CTLA-4 was not further enhanced by the addition of TH-302 during the first 10 days after treatment initiation, the triple combination therapy delayed the emergence of AR (Fig. 6 D). TH-302 monotherapy did not significantly impact tumor burden compared to isotype-treated controls; thus, the benefit of TH-302 treatment only emerged in the context of combination therapy with ICIs. TH-302 becomes activated under hypoxic conditions and is non-specifically cytotoxic to actively dividing cells in this setting (Meng et al., 2012). Therefore, TH-302 does not reduce tumor hypoxia directly, but rather it kills cells within hypoxic regions. In a prostate cancer model, TH-302 reduced the abundance of myeloid-derived suppressor cells, which accumulated in hypoxic regions (Jayaprakash et al., 2018). In contrast, T cells were not expected to be killed by TH-302 because they were excluded from hypoxic regions and had relatively lower rates of proliferation (Jayaprakash et al., 2018). Therefore, the cytotoxicity of TH-302 would be expected to primarily affect cancer and myeloid cells, but not T cells. Hypoxic regions are precisely those areas that are largely inaccessible to T cells and protected from immunotherapy-enhanced T cell–mediated killing. Therefore, the combination of ICIs and TH-302 can be envisioned as a "divide and conquer" approach, where distinct tumor regions, as defined by their oxygen tension, are susceptible to killing by either immunotherapy-boosted T cells or by the nonspecific cytotoxic activity of TH-302.

A phase I clinical trial of TH-302 in combination with anti-CTLA-4 (ipilimumab) in patients with advanced solid tumors demonstrated that the combination was well tolerated and detected anti-tumor activity, including in tumors that did not respond to ICIs, providing a strong rationale for additional clinical testing (Hegde et al., 2021). Additional agents that can reduce tumor hypoxia, such as the mitochondrial complex I inhibitor metformin, have also been combined with ICIs. Although retrospective studies of patients treated with metformin and ICIs did not identify significant improvements in progression-free or overall survival (Afzal et al., 2018; Augustin et al., 2023), case studies reporting improved clinical outcomes in patients who received metformin with ICIs (Kim et al., 2021; Wu et al., 2021), together with compelling results in murine models (Scharping et al., 2017) provide a rationale for additional clinical studies of metformin combined with ICIs (e.g., NCT04114136, NCT03994744, NCT03048500). Of note, a study of metformin combined with anti-PD-1 therapy (nivolumab) in patients with microsatellite stable metastatic colorectal cancer—a setting in which anti-PD-1 monotherapy does not provide clinical benefit (Le et al., 2015)—showed limited efficacy and was stopped (Akce et al., 2023). In future studies, it will be important to identify settings (acquired versus primary resistance to ICIs, for example) and biomarkers of sensitivity to hypoxia-targeting agents.

Tumor hypoxia, either inferred from transcriptional hypoxia signatures or from staining for carbonic anhydrase IX in patient tumors, has been associated with primary resistance to ICI therapy (Hugo et al., 2016; Zandberg et al., 2021; Najjar et al., 2019). Identifying patients with elevated tumor hypoxia during the course of ICI treatment could help to identify patients more likely to develop AR to therapy, estimated to be 50–60% of NSCLC patients who initially respond to ICIs (Gettinger et al., 2018; Schoenfeld and Hellmann, 2020; Memon et al., 2024; Ricciuti et al., 2024). Non-invasive methods to quantify tumor hypoxia, such as [^{18}F]-fluoromisonidazole (^{18}F-FMISO) positron emission tomography (PET) imaging (Lee and Scott, 2007), could be used to longitudinally monitor patients receiving ICI therapy to identify those patients in which tumor hypoxia may contribute to the development of AR; this approach has been proposed in preclinical models (Reeves et al., 2022; McNeal et al., 2024). In patients with glioblastoma treated with bevacizumab and evofosfamide (TH-302), ^{18}F-FMISO PET was employed to identify candidate circulating biomarkers of tumor hypoxia, suggesting an alternative approach to longitudinally and non-invasively monitor tumor hypoxia during the course of ICI treatment (Lodi et al., 2022).

Here, we have identified tumor hypoxia and loss of MHC-II as dominant features of tumors with AR to ICIs. Targeting hypoxic tumor regions with TH-302, a hypoxia-activated cytotoxic agent, cooperated with ICI therapy and delayed the emergence of AR. Thus, our work provides additional rationale for the potential of hypoxia-targeting approaches, specifically to delay the emergence of AR to ICIs.

Materials and methods

Generation and analysis of Msh2 KO cells

Murine lung adenocarcinoma cells LKR13 (generated by Julien Sage [Wislez et al., 2005] and generously shared by Tyler Jacks [Massachusetts Institute of Technology, Cambridge, MA, USA]) and 368T1 (generated and generously shared by Monte Winslow [Stanford University, Stanford, CA, USA] [Winslow et al., 2011]) and all genetically modified sub-lines (EV controls, LKR13-EV and 368T1-EV; and *Msh2* KO clones, LKR13-L, LKR13-H, 368T1-L, 368T1-H) were cultured at 37°C with 5% CO_2 in RPMI-1640 (21870-076; Thermo Fisher Scientific) supplemented with 10% fetal bovine serum (#16140071; FBS; Gibco) and 1% penicillin/streptomycin (#15140122; Pen/Strep; Gibco).

Msh2 KO LKR13 and 368T1 cells were generated using CRISPR/*Cas9*. Two guides (guide 1 forward: 5′-GCGCCGTGTAAAAGTCGCCG-3′; guide 1 reverse: 5′-CGGCGACTTTTACACGGCGC-3′; guide 2 forward 5′-GCGCTTCTTTGAGGGCATGC-3′; guide 2 reverse 5′-GCATGCCCTCAAAGAAGCGC-3′) targeting exon 1 of the *Msh2* gene were cloned into the Cas9 single guide RNA (sgRNA) expression vector PX458 (#48138; Addgene) that

contains a GFP reporter. An empty expression vector (EV) lacking an sgRNA was also used. LKR13 and 368T1 parental cells were transiently transfected with the EV or vectors targeting *Msh2* using Lipofectamine 2000 (#11668030; Thermo Fisher Scientific). GFP$^+$ single-cell clones were isolated via FACS 48 h after transfection with *Msh2* targeting vectors, and *Msh2* deletion was confirmed via immunoblotting. Cells were lysed in ice-cold radioimmunoprecipitation assay buffer supplemented with protease inhibitor, equal amounts of total protein were separated by gel electrophoresis on Mini-PROTEAN GTX 4–20% gels (Bio-Rad), transferred onto nitrocellulose (Bio-Rad), and probed with the following antibodies using dilutions recommended by the manufacturer: Msh2 (#2017; Cell Signaling, targeting the N-terminus); Msh2 (#70270; Abcam, targeting the C-terminus), and β-actin (#47778; Santa Cruz). Two *Msh2* KO single-cell clones each from LKR13 and 368T1 parental cells generated using independent guide sequences were selected for further analysis. In vitro proliferation assays were performed in 3T3 format, in which 3×10^5 cells were counted and plated every 3 days. Every in vivo experiment using *Msh2* KO cells was performed using cells of the same passage number that were cryopreserved in a single batch and cultured in vitro for 10–12 days prior to tumor engraftment.

For in vitro IFNγ assays, cells were incubated with 200 U/ml recombinant murine IFNγ (#485-MI-100; R&D Systems) for 48 h under either normoxic (21% O_2) or hypoxic (1% O_2) culture conditions. Single-cell suspensions were washed with phosphate-buffered saline (PBS) containing 2% FBS, then stained with the following antibodies on ice for 30 min: MHC-II:APC (#107614; BioLegend), MHC-I:PE (#114507; BioLegend) and PD-L1:PE-Cy7 (#124314; BioLegend). Flow cytometry data were acquired on an LSR II (BD) with FACSDiva and analyzed with FlowJo (TreeStar).

Animal studies

Animal studies were performed in compliance with Yale University's Institutional Animal Care and Use Committee (protocol 11364; assurance number D16-00416). 6–8-wk-old B6129SF1/J (F1; #101043; JAX stock) and B6.129S7-*Rag1*^{tm1Mom}/J (Rag1^{KO}; #002216; JAX stock) mice purchased from Jackson Laboratory and NOD SCID Il2rg$^{-/-}$ (NOD.Cg-*Prkdcscid Il2rgtm1Wjl*/SzJ or NSG; #005557; JAX stock) mice bred from Jackson Laboratory stocks were housed in a specific pathogen–free facility. 500,000 LKR13-EV, LKR13-L, LKR13-H, 368T1-EV, 368T1-L, or 368T1-H cells in 100 µl sterile PBS were injected subcutaneously into the right flanks of mice. Tumor lengths (L) and widths (W) were measured using calipers and volumes (V) were calculated using the formula $V = 0.52 \times L \times W^2$. Tumors were measured at least twice a week starting on day 6 after engraftment. Mice were randomized to treatment groups once their mean tumor volume reached between 30 and 50 mm^3 (day 10 after tumor engraftment unless otherwise noted).

Treatments

Mice were treated twice weekly via intraperitoneal (i.p.) injection with 250 µg of the following monoclonal antibodies from BioXCell: anti-PD-1 clone RMP1-14 (#BE0146); anti-CTLA-4 clone 9H10 (#BE0131); IgG2a Iso for anti-PD-1 (#BE0089); or polyclonal Syrian hamster IgG Iso for anti-CTLA-4 (#BE0087). TH-302 (#ATE448430720; Sigma-Aldrich) was delivered continuously every other day via i.p. injection at 50 mg/kg (Liu et al., 2012; Jayaprakash et al., 2018). To detect hypoxia, tumor-bearing animals were injected with 80 mg/kg pimonidazole (#HP-200; Hypoxyprobe) via i.p. injection 90 min prior to sacrifice.

For immune depletion studies, mice were treated twice weekly via i.p. injection with 200 µg of the following antibodies from BioXCell: anti-CD4 clone GK1.5 (#BE0003-1) to deplete CD4$^+$ T cells, anti-CD8 clone 53-6.7 (#BE0004-1) to deplete CD8$^+$ T cells, and anti-IFNγ clone XMG1.2 (#BP0055) to neutralize IFNγ. To confirm CD4$^+$ and CD8$^+$ T cell depletion, splenic and tumor-infiltrating lymphocytes were analyzed via flow cytometry.

Re-transplantation experiments and isolation of AR cell lines

Tumors from mice that had developed AR to anti-PD-1 alone or anti-PD-1 + anti-CTLA-4 were collected on day 39 after engraftment. Half of the tumor volume was minced and enzymatically disrupted to produce a single-cell suspension from which CD45$^-$ tumor (and stromal) cells were isolated via FACS (see flow cytometry details below). To establish AR tumor-derived cell lines, the sorted cells were plated in RPMI-1640 supplemented with 10% FBS and 1% Pen/Strep. For re-transplantation experiments, sorted AR tumor cells were resuspended in 100 µl sterile PBS and injected subcutaneously into the right flank of tumor-naïve mice. The remaining AR tumor half was dissected into ∼2 mm^3 pieces and implanted subcutaneously into the right flank of tumor-naïve mice. Once the transplanted AR tumors reached an average volume of 30–50 mm^3 (day 7 for AR tumor pieces, day 13 for dissociated AR tumor cells), mice were treated with therapeutic antibodies. Re-transplanted tumors derived from AR to anti-PD-1 tumors were treated with either anti-PD-1 or Iso, and re-transplanted tumors derived from AR to anti-PD-1 + anti-CTLA-4 tumors were treated with either anti-PD-1 + anti-CTLA-4 or Iso.

WES

Genomic DNA was isolated from tumor cell lines after in vitro culture and from in vivo tumors flash-frozen in liquid nitrogen and then crushed. Library preparation and sequencing was performed by the Yale Center for Genome Analysis (YCGA). Whole-exome libraries were prepared using the SeqCap EZ Mouse exome capture system (Roche) followed by 100 bp paired-end sequencing on the Illumina HiSeq4000 platform or the NovaSeq 6000 S2 platform with a target coverage of 150x. Raw sequencing reads were mapped to the mouse reference genome (GRCm38 build) using BWA-MEM followed by the Genome Analysis Toolkit (GATK) Best Practices workflow. SNVs and indels were called using Mutect2. *Msh2* KO samples (in vitro cultured cell lines and in vivo tumors) were compared to *Msh2* WT EV control cells to obtain the SNVs relative to the EV controls. Likely damaging variants were annotated including premature termination, canonical splice site, frameshift insertion/deletion, and missense mutation using Annovar.

Immunophenotyping via flow cytometry

Tumor tissue was minced in RPMI1640 with 2% FBS, 200 U/ml collagenase IV (#S5138; Sigma-Aldrich), and 1 µg/ml DNase (#D5025; Sigma-Aldrich) and digested at 37°C for 30 min. Samples were filtered through a 70-µm cell strainer, incubated with ammonium-chloride-potassium lysing buffer for 3 min, washed with PBS, and resuspended in RPMI1640 with 2% FBS. For intracellular cytokine staining after ex vivo stimulation with phorbol-12-myristate 13-acetate (PMA) and ionomycin, single-cell suspensions were incubated in RPMI1640 with 10% FBS and Brefeldin A (Thermo Fisher Scientific) at 37°C for 5 h. For ex vivo 2-NBDG staining, single-cell suspensions were washed in PBS and incubated in 290 µM 2-NBDG (#235976; Abcam) at 37°C for 20 min. Single-cell suspensions were washed using PBS with 2% FBS, incubated with α-FcγRIII/II antibody (2.4G2) on ice for 15 min, and then stained on ice for 30 min. For intracellular staining, samples were fixed and permeabilized with the Foxp3/Transcription Factor Staining Buffer Set (Thermo Fisher Scientific) and then stained on ice for 45 min. The following antibodies were used for surface staining: CD45:BV711 (#103147; 1:400 dilution; BioLegend), CD3:APC-Cy7 (#100222; 1:100; BioLegend), CD4:BUV737 (#612761; 1:200; BD Biosciences), CD8:BV605 (#563152; 1:200; BD Biosciences), CD44:PerCP (#103035; 1:200; BioLegend), MHC-I:PE (#114507; 1:200; BioLegend), MHC-II:APC (#107614; 1:200; BioLegend), and PD-L1:PE-Cy7 (#124314; 1:200; BioLegend). The following antibodies were used for intracellular staining: Foxp3:APC (#17-5773-82; 1:100; eBioscience), IFNγ:PE-Cy7 (#505826; 1:100; BioLegend), and anti-pimonidazole:FITC (#HP2; 1:100; Hypoxyprobe). Dead cells were excluded using Live/Dead Red Fixable Viability Dye (#L34973; 1:2,000; Thermo Fisher Scientific). Flow cytometry data were acquired on an LSR II (BD) with FACSDiva and analyzed with FlowJo (TreeStar).

scRNAseq

Sample preparation

LKR13-H tumors treated with Iso, and tumors responding to anti-PD-1 or anti-PD-1 + anti-CTLA-4 were collected on day 16 after engraftment. Tumors that had developed AR to anti-PD-1 or anti-PD-1 + anti-CTLA-4 were collected on day 39 after engraftment (late AR timepoint). Tumors were processed to generate single-cell suspensions as described for flow cytometry experiments and stained with the following antibodies: CD45:PacificBlue (#103126; 1:500; BioLegend), CD8:PE (#100512; 1:100; BioLegend), CD4:PE (#100708; 1:100; BioLegend), and CD3:APC-Cy7 (1:50). Dead cells were excluded using Live/Dead Red Fixable Viability Dye (1:500). $CD45^+CD3^+CD4/8^+$ T cells, $CD45^+CD3^-CD4/8^-$ other immune cells, and $CD45^-$ cancer (and stromal) cells were sorted on a FACSAria (BD) into RPMI-1640 supplemented with 2% FBS. For each individual tumor, the three sorted cell populations—T cells, other immune cells, and $CD45^-$ cancer (and stromal) cells—were combined at a 2:1:1 ratio.

Sequencing

An equal number of cells from three mice per experimental condition were pooled and 17,000 cells from each condition were loaded on the 10x Genomics Chromium System. Library preparation and sequencing was performed at YCGA. Library preparation was performed using 10x Genomics reagents according to the manufacturer's instructions, and sequencing was performed with a target of 300 million reads per sample (target 10,000 cells) on the Illumina NovaSeq 6000 platform.

Data analysis

Cell Ranger was used to generate fastq files from raw call files, align reads to the mm10 reference genome, filter reads, and aggregate the cell-by-gene matrices for each individual sample. Seurat (v4.0.3) was used to process, analyze, and visualize the data. The data were filtered to include only cells with <15% mitochondrial reads and >100 genes, and genes expressed in >10 cells. Raw reads were normalized and the top 3,000 variable genes were identified using the Seurat SCTransform function while regressing mitochondrial content. Principal component analysis was performed on the most variable genes, followed by graph-based clustering using the FindClusters function to generate clusters that were visualized using the dimension reduction method Uniform Manifold Approximation Projection (UMAP) using the first 50 principal components. Clusters containing cancer cells, lymphocytes, and myeloid cells were identified via the expression of cell lineage marker genes (shown in Fig. S2 B). Cancer cells, lymphocytes, and myeloid cells were subsetted, doublets were removed based on co-expression of cell markers, and the data were re-analyzed with SCTransform while regressing for batch. Cluster frequencies by sample were normalized to the number of cells per sample and stacked column plots were generated using ggplot2 (v3.3.5). Mean scaled expression values of each gene were calculated per cluster, and heatmaps were generated with values scaled by gene using pheatmap (v1.0.12).

To calculate DEGs, cancer cell and lymphocyte counts were log-normalized and scaled using the Seurat NormalizeData and ScaleData functions, followed by the FindAllMarkers function to identify DEGs in each cluster and in each sample. GSEA using the preranked method was performed using the top DEGs across different cancer cell and lymphocyte samples with the GO and Hallmark gene sets. Gene sets that were significantly enriched (FDR q value <0.25; P value <0.05) in both AR to anti-PD-1 and AR to anti-PD-1 + anti-CTLA-4 cancer cell samples, as well as gene sets that were significantly enriched in both responding to anti-PD-1 and responding to anti-PD-1 + anti-CTLA-4 cancer cell samples, were considered for downstream analysis (Table S1).

Immunofluorescence and immunohistochemistry

Tumors were dissected into 4% paraformaldehyde (Electron Microscopy Services), fixed overnight at room temperature, and then rehydrated in 70% ethanol. Yale Pathology Tissue Services produced paraffin-embedded sections according to standard methods. After citrate-based antigen retrieval, immunofluorescence staining was performed with anti-pimonidazole:FITC and rabbit anti-CD3 (Spring Biosciences) antibodies overnight at 4°C and fluorescent secondary antibody for 1 h at room temperature (anti-rabbit AlexaFluor594; Thermo Fisher Scientific). Total DNA was stained with Hoechst-33342 (Thermo Fisher Scientific). Images were acquired on an inverted

widefield microscope (Zeiss). QuPath was used to measure tumor hypoxia based on the percentage pimonidazole positive area per FOV quantified using a FITC signal intensity threshold. $CD3^+$ T cells were quantified using the cell detection algorithm in QuPath followed by an AlexaFluor594 signal intensity threshold. To quantify the percentage of T cells contained within either normoxic or hypoxic areas, only FOV in which a hypoxic area was identified and contained at least 10 cells were considered. The percentage of T cells contained within either normoxic or hypoxic areas, as well as the overall T cell abundance, was calculated for each individual FOV. Immunohistochemistry was performed after citrate-based antigen retrieval for staining with rabbit anti-HMGB1 (#6893, 1:200 dilution; Cell Signaling Technology) or Tris/EDTA-based antigen retrieval for staining with recombinant anti-Bcl-2 (#ab182858, 1:500 dilution; Abcam). Images were acquired on an inverted widefield microscope (Zeiss) and QuPath was used to quantify the percentage of positive cells and the mean cell intensity.

Analysis of NSCLC patient RNAseq data

We derived a hypoxia metagene signature from those genes within the Hallmark Hypoxia gene set that were significantly enriched in both murine LKR13-H tumors that developed AR to anti-PD-1 and to anti-PD-1 + anti-CTLA-4. This corresponds to a subset of the genes shown in Fig. 5 A, which encompass genes significantly enriched in either treatment group. We then turned to RNAseq data from 152 NSCLC patients treated with ICIs from the SU2C-MARK cohort, which was analyzed as in Ravi et al. (2023). For the genes in the hypoxia signature, we took the mean of the $\log_2$-transformed transcripts per million (TPMs) and compared samples to each other by z-scoring the averages. We then compared z-scores across the best objective response (BOR) groupings of PR/CR, SD, or PD. Survival analysis was performed using progression-free and overall survival data. Patients were binned into high and low hypoxia metagene expression categories using the median expression level as the cut-point.

Immunopeptidomics

The following antibodies were used for the immunopurification (all from BioXcell): anti-Mouse H2 (M1/42.3.9.8) MHC class I (BE0077) and anti-Mouse H2-IAd/IEd (M5/114) MHC class II (BE0108). Polyprep chromatography column (#7311553; Bio-Rad), CNBr activated sepharose 4B (#45000066; Fisher), Dynamag-2 (#12321D; Invitrogen), 1.5 ml Protein LoBind from Eppendorf, (022431081; Fisher), 2 ml Protein LoBind from Eppendorf (#02243100; Fisher), 2.0 ml Costar microfuge tubes, 2 ml (3213; Corning) 15 ml Falcon tubes (352096; Corning), solid phase extraction disk, ultramicrospin column C18 (the nest group, #SEMSS18V, 5–200 µl), low retention tips: EPLORET reload tip 10, 200, 1,000 µl (#2717349, #2717351, #2717352; Fisher). Acetonitrile (ACN, #A9964), trifluoroacetic acid (TFA, #AA446305Y), formic acid (FA, #AC147930010), chaps (#22020110GM), PBS (Buph, phosphate buffer saline packs, #28372), ammonium bicarbonate (#A643-500), sodium deoxycholate (#89905), and phenyl-methylsulfonyl fluoride (#AAB2214603) were purchased from Fisher. Combined inhibitor EDTA-free (#A32961) was purchased from Bio-Rad.

Cell lysis

Three biological replicates of 1×10^8 cells for each cell line were collected and washed twice with PBS and dried pellets were stored at −80°C until use. Cell pellets were gently thawed and resuspended with 0.5 ml cold PBS. The total volume (cells in PBS) was measured and the equivalent volume of 2x cell lysis buffer (1% chaps in PBS and 1 pellet/10 ml of combined inhibitor EDTA-free, 2 mM phenyl- methylsulfonyl fluoride, 2% octyl-β-d glucopyranoside) was added. Cell lysates were incubated and rotated for 1 h at 4°C using the Revolver apparatus (20 RPM). Cleared cell lysates were harvested following 20 min by centrifugation at 17,927 RCF (13,000 RPM) at 4°C (fixed rotor). Supernatants were transferred into new 2.0-ml tubes and kept on ice.

Bead coupling and immunoprecipitation

MHC class I and II peptides were immunopurified as in Sirois et al. (2021). Briefly, 80 mg of sepharose CNBr-activated beads were coupled with 2 mg of antibody. Sepharose antibody-coupled beads were incubated with the cell lysate overnight at 4°C using a slow rotating wheel Revolver apparatus (22 RPM). Immunocapture of MHC class I and MHC class II complexes using the antibody-coupled beads was performed serially. First, cell lysates were incubated with the MHC class I antibody-coupled beads at 4°C overnight. Then, the mixture was transferred into a BIO-Rad column. The flowthrough (cell lysate depleted of MHC class I complexes) was recovered and re-incubated overnight at 4°C with MHC class II coupled beads. Then, the antibody-coupled beads were washed sequentially using the Bio-Rad columns with 10 ml of buffer A (150 mM NaCl and 20 mM Tris–HCl pH 8), 10 ml of buffer B (400 mM NaCl and 20 mM Tris–HCl pH 8), 10 ml of buffer A, and 10 ml of buffer C (20 mM Tris–HCl pH 8.). MHC-ligand complexes were eluted from the beads with 2 × 300 µl of 1% TFA. MHC-ligands were eluted using C18 columns pre-conditioned with 200 µl of methanol followed by 80% acetonitrile/0.1% TFA and spin at 1,545 RCF in a fixed rotor. The flowthrough was aspirated and 200 µl of 0.1% TFA was added to the column and spun again. 3 × 200 µl of the MHC-ligand complexes solution was loaded into the column followed by a wash (200 µl) with 0.1% TFA and spin. The stage tips were transferred onto a 2.0 ml Eppendorf tube and peptides were eluted with 3 × 200 µl of 28% ACN-0.1% TFA. The flowthrough containing the eluted peptides was stored at −20°C for MS analysis.

Liquid chromatography with tandem mass spectrometry (LC-MSMS) analysis and peptide identification

Samples were solubilized in 4% FA. Each biological replicate was divided into three technical replicates for LC-MSMS analysis and loaded on a home-made reversed-phase column (150-µm i.d. by 250-mm length, Jupiter 3 µm C18 300 Å) with a gradient from 5 to 30% ACN-0.1% FA and a 600 nl/min flow rate on an Easy nLC-1200 connected to an Orbitrap Eclipse (Thermo Fisher Scientific). Each full MS spectrum was acquired at a resolution of 120,000, an automatic gain control (AGC) of 4E5 with automatic mode for the injection time. It was followed by tandem-MS (MS-MS) spectra acquisition on the most abundant multiply charged precursor ions for a maximum of 3 s. Tandem-MS

experiments were performed using higher energy collisional dissociation at a collision energy of 30%, a resolution of 30,000, an AGC of 1.5E5, and an injection time of 300 ms. Data files were processed using PEAKS X software (Peaks Pro V10.6; Bioinformatics Solutions) using the mouse database UniProtKB/Swiss-Prot (2019_09) for self-antigens. "Unspecified enzyme digestion" was selected for the enzyme parameter and mass tolerances on precursor and fragment ions were 10 ppm and 0.01 Da, respectively. Variable modifications were deamidation (NQ) and oxidation (M). All other search parameters were the default values. Final peptide lists were filtered using average local confidence (ALC) of 80% and with an FDR of 1% using the Peaks software. Data were visualized using MVP software (https://github.com/CaronLab/MhcVizPipe) (Kovalchik et al., 2022).

Statistical analysis

Statistical analyses for murine model experiments were performed using GraphPad Prism (v9.2.0). One-way or two-way ANOVA with multiple comparison testing, or two-tailed paired or unpaired Students *t* test, was used to determine statistical significance (*P < 0.05, **P < 0.01, ***P < 0.001, ****P < 0.0001) as indicated in the figure legends.

Online supplemental material

Fig. S1 shows the CRISPR/Cas9-mediated KO of Msh2; 368T1 and LKR13 tumor growth curves in immunocompetent, $Rag1^{KO}$, and NSG mice; surface expression of MHC-I and PD-L1 in 368T1 and LKR13 cells with and without IFNγ treatment; surface expression of PD-L1 in $CD45^-$ cancer (and stromal) cells isolated from 368T1 and LKR13 tumors; and SNVs identified in isotype treated LKR13-H tumors and those with AR to anti-PD-1 or anti-PD-1 + anti-CTLA-4. Fig. S2 shows UMAPs of cells isolated from LKR13-H tumors; UMAPs depicting expression of genes that were used to support cell-type assignments; heatmaps of selected genes in lymphocyte and myeloid clusters; and barplots showing the abundance of cells per cluster from each treatment condition. Fig. S3 shows a barplot of the abundance of cancer cells per cluster from each treatment condition; GSEA profiles enriched in cancer cells from tumors that were responding to anti-PD-1 or anti-PD-1 + anti-CTLA-4 or that had developed AR to these treatments; surface expression of PD-L1 in $CD45^-$ cancer (and stromal) cells isolated from tumors that were responding or had developed resistance to ICIs, or were isotype-treated; abundance of $CD8^+$ and $CD4^+$ T cells isolated from tumors treated with isotype or anti-PD-1 + anti-CTLA-4 and with either anti-CD4, anti-CD8, or anti-IFNγ antibodies; and surface expression of MHC-I and PD-L1 in LKR13-H cells and four cell lines derived from LKR13-H tumors that developed AR to ICIs, with and without IFNγ treatment. Fig. S4 shows a surface expression of MHC-I and MHC-II in LKR13-H cells and two cell lines derived from LKR13-H tumors that developed AR to ICIs, with and without IFNγ treatment; the length distribution of eluted peptides bound to MHC-I and MHC-II identified via immunopeptidomics from IFNγ-treated cells; heatmaps showing the number of peptides with binding affinity scores for MHC-I and MHC-II alleles; and peptide binding motifs based on unsupervised GibbsCluster analysis. Fig. S5 shows expression of selected hypoxia-related genes in cancer cells from tumors that were responding or had developed resistance to ICIs, or were isotype-treated; volumes of tumors that were isotype-treated or tumors with AR to ICIs collected on day 26, corresponding to the early AR timepoint; immunofluorescence staining of hypoxia (via pimonidazole) and T cells (via CD3) in tumors that were responding or had developed resistance to ICIs, or were isotype-treated; surface MHC-II and MHC-I expression in LKR13-EV, LKR13-H, and two cell lines derived from LKR13-H tumors that developed AR to ICIs, with and without IFNγ treatment and under normoxic or hypoxic conditions; and the following in LKR13-H tumors treated with Iso or anti-PD-1 + anti-CTLA-4 and/or TH-302: abundance and FNγ production of $CD8^+$ and $CD4^+$ T cells, abundance of $Foxp3^+$ Tregs, surface expression of MHC-II in $CD45^-$ cancer (and stromal) cells, representative immunohistochemistry images and quantification of expression levels of Bcl-2 and HMGB1, and quantification of pimonidazole immunofluorescence staining. Table S1 shows significantly enriched GO and Hallmark gene sets in cancer cells from LKR13-H tumors that were responding or developed AR to ICIs.

Data availability

The murine WES data in this study, underlying Figs. 1 and S1, are available in Sequence Read Archive at PRJNA1153947. The patient WES data underlying Fig. 6, published in Ravi et al. (2023), are available in dbGaP (phs002822.v1.p1). The murine scRNAseq data in this study, underlying Figs. 3, 4, 5, S2, S3, and S5, are available in the Gene Expression Omnibus at GSE275877. Other data can be found in the paper or its online supplemental material.

Acknowledgments

We thank members of the Politi and Kaech laboratories for helpful discussion and feedback, Nikhil Joshi for careful reading of the manuscript, Ruslan Medzhivtov for kindly providing access to a hypoxia chamber, and Kurt Schalper for assistance with immunofluorescence staining methods.

This work was supported by the National Institute of Health (NIH), National Cancer Institute (NCI) R01 CA195720 to K. Politi and S.M. Kaech. C. Robles-Oteíza is supported by NCI F99/K00 CA245819. K. Hastings was supported by NCI F32 CA210516. A. Ravi is supported by NCI K99/R00 CA245897. F. de Miguel was supported by the Yale Cancer Biology Training Program (NIH T32 CA193200-01A1). This research was supported by the National Research Foundation of Korea grants funded by the South Korean government (2022R1A4A2000827) to J. Choi. Funding for this study was also provided by a Stand Up To Cancer – American Cancer Society Lung Cancer Dream Team Translational Research Grant (Grant Number: SU2C-AACR-DT17-15, Consortium Award). Stand Up to Cancer is a program of the Entertainment Industry Foundation. Research grants are administered by the American Association for Cancer Research, the scientific partner of Stand Up To Cancer. This work was additionally supported by The Mark Foundation for Cancer Research (Grant Number: 19-029-MIA, Consortium Award) Expanding Therapeutic Options for Lung Cancer project.

Author contributions: C. Robles-Oteíza: Conceptualization, Data curation, Formal analysis, Investigation, Methodology, Software, Validation, Visualization, Writing – original draft, Writing – review & editing, K. Hastings: Conceptualization, Data curation, Investigation, Methodology, J. Choi: Formal analysis, Methodology, Visualization, Writing – original draft, I. Sirois: Investigation, Methodology, Visualization, A. Ravi: Data curation, Formal analysis, Investigation, Visualization, F. Expósito: Formal analysis, Investigation, Methodology, Software, Visualization, Writing – review & editing, F. de Miguel: Conceptualization, Investigation, Resources, J.R. Knight: Formal analysis, Software, F. López-Giraldez: Formal analysis, H. Choi: Investigation, Writing – review & editing, N.D. Socci: Formal analysis, Software, T. Merghoub: Conceptualization, Funding acquisition, Project administration, Resources, M. Awad: Data curation, Formal analysis, Funding acquisition, Project administration, Writing – review & editing, G. Getz: Resources, Supervision, J. Gainor: Resources, Writing – review & editing, M.D. Hellmann: Data curation, Resources, Writing – review & editing, E. Caron: Supervision, S.M. Kaech: Investigation, Validation, Writing – review & editing, K. Politi: Conceptualization, Funding acquisition, Project administration, Supervision, Writing – original draft, Writing – review & editing

Disclosures: A. Ravi reported "other" from Halo Solutions outside the submitted work. F. Expósito reported being supported by the Fundación Ramón Areces Life and Matter Sciences Postdoctoral Fellowship and the 2023 LCRF leading edge Research Grant Program. N.D. Socci reported grants from NIH during the conduct of the study. T. Merghoub reported being a consultant for Immunos Therapeutics, Daiichi Sankyo Co, TigaTX, Normunity, and Pfizer. T. Merghoub is a cofounder of and equity holder in Imvaq Therapeutics. T. Merghoub receives research grant funding from Bristol Myers Squibb, Surface Oncology, Kyn Therapeutics, Infinity Pharmaceuticals, Peregrine Pharmaceuticals, Adaptive Biotechnologies, Leap Therapeutics, and Aprea Therapeutics. T. Merghoub is an inventor on patent applications related to work on oncolytic viral therapy, alpha virus-based vaccine, neo-antigen modeling, CD40, GITR, OX40, PD-1, and CTLA-4. M. Awad reported personal fees from Genentech, Bristol-Myers Squibb, Merck, AstraZeneca, Lilly, Mirati, Gritstone, EMD Serono, Regeneron, Janssen, Affini-T, Novartis, Coherus, D3Bio, and AbbVie; and grants from Amgen, Lilly, Bristol-Myers Squibb, Genentech, and AstraZeneca outside the submitted work. G. Getz reported research funds from IBM, Pharmacyclics/Abbvie, Bayer, Genentech, Calico, and Ultima Genomics, and is also an inventor on patent applications filed by the Broad Institute related to MSMuTect, MSMutSig, POLYSOLVER, SignatureAnalyzer-GPU, MSEye, and MinimuMM-seq. G. Getz is a founder and consultant, and holds privately held equity in Scorpion Therapeutics; he is also a founder of, and holds privately held equity in, PreDICTA Biosciences. He was also a consultant to Merck. J. Gainor reported grants from Stand Up To Cancer and grants from Mark Foundation during the conduct of the study; personal fees from Bristol-Myers Squibb, Merck, Genentech/Roche, AstraZeneca, Loxo/Lilly, Mariana Therapeutics, Pfizer, Mirati Therapeutics, iTeos, Novartis, Merus Pharmaceuticals, AI proteins, Novocure, Silverback Therapeutics, Beigene, Takeda, and Sanofi; and grants from Moderna outside the submitted work; and that an immediate family member is an employee with equity in Ironwood Pharmaceuticals. M.D. Hellmann reported "other" from AstraZeneca outside the submitted work; and is an employee and stock holder of AstraZeneca. S.M. Kaech reported personal fees from EvolveImmune Therapeutics, Simcha Therapeutics, Siren Biotechnology, and Arvinas; and grants from Arvinas and Takeda during the conduct of the study. K. Politi reported grants from AstraZeneca, Roche/Genentech, Boehringer Ingelheim, and D2G Oncology; and personal fees from AstraZeneca and Revelio Therapeutics, Inc outside the submitted work; in addition, K. Politi had a patent to related to EGFR T790M mutation testing with royalties paid "from MSKCC/MolecularMD"; and serves on the AACR Board of Directors and the Lung Cancer Research Foundation Board of Directors. K. Politi is also a co-founder of and consultant for Revelio Therapeutics, Inc. No other disclosures were reported.

Submitted: 28 June 2023
Revised: 29 April 2024
Accepted: 27 September 2024

References

Afzal, M.Z., R.R. Mercado, and K. Shirai. 2018. Efficacy of metformin in combination with immune checkpoint inhibitors (anti-PD-1/anti-CTLA-4) in metastatic malignant melanoma. *J. Immunother. Cancer*. 6:64. https://doi.org/10.1186/s40425-018-0375-1

Akce, M., B. Farran, J.M. Switchenko, M. Rupji, S. Kang, L. Khalil, A. Ruggieri-Joyce, B. Olson, W.L. Shaib, C. Wu, et al. 2023. Phase II trial of nivolumab and metformin in patients with treatment-refractory microsatellite stable metastatic colorectal cancer. *J. Immunother. Cancer*. 11: e007235. https://doi.org/10.1136/jitc-2023-007235

Augustin, R.C., Z. Huang, F. Ding, S. Zhai, J. McArdle, A. Santisi, M. Davis, C. Sander, D. Davar, J.M. Kirkwood, et al. 2023. Metformin is associated with improved clinical outcomes in patients with melanoma: A retrospective, multi-institutional study. *Front. Oncol.* 13:1075823. https://doi.org/10.3389/fonc.2023.1075823

Axelrod, M.L., R.S. Cook, D.B. Johnson, and J.M. Balko. 2019. Biological consequences of MHC-II expression by tumor cells in cancer. *Clin. Cancer Res.* 25:2392–2402. https://doi.org/10.1158/1078-0432.CCR-18-3200

Ayers, M., J. Lunceford, M. Nebozhyn, E. Murphy, A. Loboda, D.R. Kaufman, A. Albright, J.D. Cheng, S.P. Kang, V. Shankaran, et al. 2017. IFN-γ-related mRNA profile predicts clinical response to PD-1 blockade. *J. Clin. Invest.* 127:2930–2940. https://doi.org/10.1172/JCI91190

Barsoum, I.B., M. Koti, D.R. Siemens, and C.H. Graham. 2014. Mechanisms of hypoxia-mediated immune escape in cancer. *Cancer Res.* 74:7185–7190. https://doi.org/10.1158/0008-5472.CAN-14-2598

Baumeister, S.H., G.J. Freeman, G. Dranoff, and A.H. Sharpe. 2016. Coinhibitory pathways in immunotherapy for cancer. *Annu. Rev. Immunol.* 34:539–573. https://doi.org/10.1146/annurev-immunol-032414-112049

Bhandari, V., C. Hoey, L.Y. Liu, E. Lalonde, J. Ray, J. Livingstone, R. Lesurf, Y.J. Shiah, T. Vujcic, X. Huang, et al. 2019. Molecular landmarks of tumor hypoxia across cancer types. *Nat. Genet.* 51:308–318. https://doi.org/10.1038/s41588-018-0318-2

Borghaei, H., L. Paz-Ares, L. Horn, D.R. Spigel, M. Steins, N.E. Ready, L.Q. Chow, E.E. Vokes, E. Felip, E. Holgado, et al. 2015. Nivolumab versus docetaxel in advanced nonsquamous non-small-cell lung cancer. *N. Engl. J. Med.* 373:1627–1639. https://doi.org/10.1056/NEJMoa1507643

Boumelha, J., S. de Carné Trécesson, E.K. Law, P. Romero-Clavijo, M.A. Coelho, K.W. Ng, E. Mugarza, C. Moore, S. Rana, D.R. Caswell, et al. 2022. An immunogenic model of KRAS-mutant lung cancer enables evaluation of targeted therapy and immunotherapy combinations. *Cancer Res.* 82:3435–3448. https://doi.org/10.1158/0008-5472.CAN-22-0325

Brahmer, J., K.L. Reckamp, P. Baas, L. Crinò, W.E. Eberhardt, E. Poddubskaya, S. Antonia, A. Pluzanski, E.E. Vokes, E. Holgado, et al. 2015. Nivolumab versus docetaxel in advanced squamous-cell non-small-cell lung cancer. *N. Engl. J. Med.* 373:123–135. https://doi.org/10.1056/NEJMoa1504627

Cascone, T., J.A. McKenzie, R.M. Mbofung, S. Punt, Z. Wang, C. Xu, L.J. Williams, Z. Wang, C.A. Bristow, A. Carugo, et al. 2018. Increased tumor glycolysis characterizes immune resistance to adoptive T cell therapy. *Cell Metab.* 27:977–987.e4. https://doi.org/10.1016/j.cmet.2018.02.024

Cavadas, M.A., M. Mesnieres, B. Crifo, M.C. Manresa, A.C. Selfridge, C.C. Scholz, E.P. Cummins, A. Cheong, and C.T. Taylor. 2015. REST mediates resolution of HIF-dependent gene expression in prolonged hypoxia. *Sci. Rep.* 5:17851. https://doi.org/10.1038/srep17851

Chandrasekaran, S., M. Sasaki, C.D. Scharer, H.T. Kissick, D.G. Patterson, K.R. Magliocca, J.T. Seykora, B. Sapkota, D.A. Gutman, L.A. Cooper, et al. 2019. Phosphoinositide 3-kinase signaling can modulate MHC class I and II expression. *Mol. Cancer Res.* 17:2395–2409. https://doi.org/10.1158/1541-7786.MCR-19-0545

Cristescu, R., R. Mogg, M. Ayers, A. Albright, E. Murphy, J. Yearley, X. Sher, X.Q. Liu, H. Lu, M. Nebozhyn, et al. 2018. Pan-tumor genomic biomarkers for PD-1 checkpoint blockade-based immunotherapy. *Science.* 362:eaar3593. https://doi.org/10.1126/science.aar3593

Datar, I.J., S.C. Hauc, S. Desai, N. Gianino, B. Henick, Y. Liu, K. Syrigos, D.L. Rimm, P. Kavathas, S. Ferrone, and K.A. Schalper. 2021. Spatial analysis and clinical significance of HLA class-I and class-II subunit expression in non-small cell lung cancer. *Clin. Cancer Res.* 27:2837–2847. https://doi.org/10.1158/1078-0432.CCR-20-3655

Duan, J.X., H. Jiao, J. Kaizerman, T. Stanton, J.W. Evans, L. Lan, G. Lorente, M. Banica, D. Jung, J. Wang, et al. 2008. Potent and highly selective hypoxia-activated achiral phosphoramidate mustards as anticancer drugs. *J. Med. Chem.* 51:2412–2420. https://doi.org/10.1021/jm701028q

DuPage, M., A.L. Dooley, and T. Jacks. 2009. Conditional mouse lung cancer models using adenoviral or lentiviral delivery of Cre recombinase. *Nat. Protoc.* 4:1064–1072. https://doi.org/10.1038/nprot.2009.95

Garcia-Diaz, A., D.S. Shin, B.H. Moreno, J. Saco, H. Escuin-Ordinas, G.A. Rodriguez, J.M. Zaretsky, L. Sun, W. Hugo, X. Wang, et al. 2017. Interferon receptor signaling pathways regulating PD-L1 and PD-L2 expression. *Cell Rep.* 19:1189–1201. https://doi.org/10.1016/j.celrep.2017.04.031

Gejman, R.S., A.Y. Chang, H.F. Jones, K. DiKun, A.A. Hakimi, A. Schietinger, and D.A. Scheinberg. 2018. Rejection of immunogenic tumor clones is limited by clonal fraction. *Elife.* 7:e41090. https://doi.org/10.7554/eLife.41090

Germano, G., S. Lamba, G. Rospo, L. Barault, A. Magrì, F. Maione, M. Russo, G. Crisafulli, A. Bartolini, G. Lerda, et al. 2017. Inactivation of DNA repair triggers neoantigen generation and impairs tumour growth. *Nature.* 552:116–120. https://doi.org/10.1038/nature24673

Gettinger, S., J. Choi, K. Hastings, A. Truini, I. Datar, R. Sowell, A. Wurtz, W. Dong, G. Cai, M.A. Melnick, et al. 2017. Impaired HLA class I antigen processing and presentation as a mechanism of acquired resistance to immune checkpoint inhibitors in lung cancer. *Cancer Discov.* 7:1420–1435. https://doi.org/10.1158/2159-8290.CD-17-0593

Gettinger, S.N., A. Wurtz, S.B. Goldberg, D. Rimm, K. Schalper, S. Kaech, P. Kavathas, A. Chiang, R. Lilenbaum, D. Zelterman, et al. 2018. Clinical features and management of acquired resistance to PD-1 Axis inhibitors in 26 patients with advanced non-small cell lung cancer. *J. Thorac. Oncol.* 13:831–839. https://doi.org/10.1016/j.jtho.2018.03.008

Gubin, M.M., X. Zhang, H. Schuster, E. Caron, J.P. Ward, T. Noguchi, Y. Ivanova, J. Hundal, C.D. Arthur, W.J. Krebber, et al. 2014. Checkpoint blockade cancer immunotherapy targets tumour-specific mutant antigens. *Nature.* 515:577–581. https://doi.org/10.1038/nature13988

Hatfield, S.M., J. Kjaergaard, D. Lukashev, T.H. Schreiber, B. Belikoff, R. Abbott, S. Sethumadhavan, P. Philbrook, K. Ko, R. Cannici, et al. 2015. Immunological mechanisms of the antitumor effects of supplemental oxygenation. *Sci. Transl. Med.* 7:277ra30. https://doi.org/10.1126/scitranslmed.aaa1260

Hegde, A., P. Jayaprakash, C.A. Couillault, S. Piha-Paul, D. Karp, J. Rodon, S. Pant, S. Fu, E.E. Dumbrava, T.A. Yap, et al. 2021. A phase I dose-escalation study to evaluate the safety and tolerability of evofosfamide in combination with ipilimumab in advanced solid malignancies. *Clin. Cancer Res.* 27:3050–3060. https://doi.org/10.1158/1078-0432.CCR-20-4118

Hensley, C.T., B. Faubert, Q. Yuan, N. Lev-Cohain, E. Jin, J. Kim, L. Jiang, B. Ko, R. Skelton, L. Loudat, et al. 2016. Metabolic heterogeneity in human lung tumors. *Cell.* 164:681–694. https://doi.org/10.1016/j.cell.2015.12.034

Herbst, R.S., E.B. Garon, D.W. Kim, B.C. Cho, J.L. Perez-Gracia, J.Y. Han, C.D. Arvis, M. Majem, M.D. Forster, I. Monnet, et al. 2020. Long-term outcomes and retreatment among patients with previously treated, programmed death-ligand 1–positive, advanced non–small-cell lung cancer in the KEYNOTE-010 study. *J. Clin. Oncol.* 38:1580–1590. https://doi.org/10.1200/JCO.19.02446

Hugo, W., J.M. Zaretsky, L. Sun, C. Song, B.H. Moreno, S. Hu-Lieskovan, B. Berent-Maoz, J. Pang, B. Chmielowski, G. Cherry, et al. 2016. Genomic and transcriptomic features of response to anti-PD-1 therapy in metastatic melanoma. *Cell.* 165:35–44. https://doi.org/10.1016/j.cell.2016.02.065

Ivanov, S.V., K. Salnikow, A.V. Ivanova, L. Bai, and M.I. Lerman. 2007. Hypoxic repression of STAT1 and its downstream genes by a pVHL/HIF-1 target DEC1/STRA13. *Oncogene.* 26:802–812. https://doi.org/10.1038/sj.onc.1209842

Jaiswal, A.R., A.J. Liu, S. Pudakalakatti, P. Dutta, P. Jayaprakash, T. Bartkowiak, C.R. Ager, Z.Q. Wang, A. Reuben, Z.A. Cooper, et al. 2020. Melanoma evolves complete immunotherapy resistance through the acquisition of a hypermetabolic phenotype. *Cancer Immunol. Res.* 8:1365–1380. https://doi.org/10.1158/2326-6066.CIR-19-0005

Jayaprakash, P., M. Ai, A. Liu, P. Budhani, T. Bartkowiak, J. Sheng, C. Ager, C. Nicholas, A.R. Jaiswal, Y. Sun, et al. 2018. Targeted hypoxia reduction restores T cell infiltration and sensitizes prostate cancer to immunotherapy. *J. Clin. Invest.* 128:5137–5149. https://doi.org/10.1172/JCI96268

Johnson, A.M., B.L. Bullock, A.J. Neuwelt, J.M. Poczobutt, R.E. Kaspar, H.Y. Li, J.W. Kwak, K. Hopp, M.C.M. Weiser-Evans, L.E. Heasley, et al. 2020. Cancer cell-intrinsic expression of MHC class II regulates the immune microenvironment and response to anti-PD-1 therapy in lung adenocarcinoma. *J. Immunol.* 204:2295–2307. https://doi.org/10.4049/jimmunol.1900778

Johnson, D.B., M.V. Estrada, R. Salgado, V. Sanchez, D.B. Doxie, S.R. Opalenik, A.E. Vilgelm, E. Feld, A.S. Johnson, A.R. Greenplate, et al. 2016. Melanoma-specific MHC-II expression represents a tumour-autonomous phenotype and predicts response to anti-PD-1/PD-L1 therapy. *Nat. Commun.* 7:10582. https://doi.org/10.1038/ncomms10582

Johnson, L., K. Mercer, D. Greenbaum, R.T. Bronson, D. Crowley, D.A. Tuveson, and T. Jacks. 2001. Somatic activation of the K-ras oncogene causes early onset lung cancer in mice. *Nature.* 410:1111–1116. https://doi.org/10.1038/35074129

Kalbasi, A., M. Tariveranmoshabad, K. Hakimi, S. Kremer, K.M. Campbell, J.M. Funes, A. Vega-Crespo, G. Parisi, A. Champekar, C. Nguyen, et al. 2020. Uncoupling interferon signaling and antigen presentation to overcome immunotherapy resistance due to JAK1 loss in melanoma. *Sci. Transl. Med.* 12:eabb0152. https://doi.org/10.1126/scitranslmed.abb0152

Kerbel, R.S. 2008. Tumor angiogenesis. *N. Engl. J. Med.* 358:2039–2049. https://doi.org/10.1056/NEJMra0706596

Kim, Y., E. Vagia, P. Viveiros, C.Y. Kang, J.Y. Lee, G. Gim, S. Cho, H. Choi, L. Kim, I. Park, et al. 2021. Overcoming acquired resistance to PD-1 inhibitor with the addition of metformin in small cell lung cancer (SCLC). *Cancer Immunol. Immunother.* 70:961–965. https://doi.org/10.1007/s00262-020-02703-8

Kovalchik, K.A., Q. Ma, L. Wessling, F. Saab, J.D. Duquette, P. Kubiniok, D.J. Hamelin, P. Faridi, C. Li, A.W. Purcell, et al. 2022. MhcVizPipe: A quality control software for rapid assessment of small- to large-scale immunopeptidome datasets. *Mol. Cell. Proteomics.* 21:100178. https://doi.org/10.1016/j.mcpro.2021.100178

Kverneland, A.H., C. Enevold, M. Donia, L. Bastholt, I.M. Svane, and C.H. Nielsen. 2018. Development of anti-drug antibodies is associated with shortened survival in patients with metastatic melanoma treated with ipilimumab. *OncoImmunology.* 7:e1424674. https://doi.org/10.1080/2162402X.2018.1424674

Le, D.T., J.N. Durham, K.N. Smith, H. Wang, B.R. Bartlett, L.K. Aulakh, S. Lu, H. Kemberling, C. Wilt, B.S. Luber, et al. 2017. Mismatch repair deficiency predicts response of solid tumors to PD-1 blockade. *Science.* 357:409–413. https://doi.org/10.1126/science.aan6733

Le, D.T., J.N. Uram, H. Wang, B.R. Bartlett, H. Kemberling, A.D. Eyring, A.D. Skora, B.S. Luber, N.S. Azad, D. Laheru, et al. 2015. PD-1 blockade in tumors with mismatch-repair deficiency. *N. Engl. J. Med.* 372:2509–2520. https://doi.org/10.1056/NEJMoa1500596

Lee, S.T., and A.M. Scott. 2007. Hypoxia positron emission tomography imaging with 18f-fluoromisonidazole. *Semin. Nucl. Med.* 37:451–461. https://doi.org/10.1053/j.semnuclmed.2007.07.001

Lin, Q., X. Cong, and Z. Yun. 2011. Differential hypoxic regulation of hypoxia-inducible factors 1alpha and 2alpha. *Mol. Cancer Res.* 9:757–765. https://doi.org/10.1158/1541-7786.MCR-11-0053

Liu, Q., J.D. Sun, J. Wang, D. Ahluwalia, A.F. Baker, L.D. Cranmer, D. Ferraro, Y. Wang, J.X. Duan, W.S. Ammons, et al. 2012. TH-302, a hypoxia-activated prodrug with broad in vivo preclinical combination therapy efficacy: Optimization of dosing regimens and schedules. *Cancer*

Chemother. Pharmacol. 69:1487–1498. https://doi.org/10.1007/s00280-012-1852-8

Lodi, A., R. Pandey, J. Chiou, A. Bhattacharya, S. Huang, X. Pan, B. Burgman, S.S. Yi, S. Tiziani, and A.J. Brenner. 2022. Circulating metabolites associated with tumor hypoxia and early response to treatment in bevacizumab-refractory glioblastoma after combined bevacizumab and evofosfamide. *Front. Oncol.* 12:900082. https://doi.org/10.3389/fonc.2022.900082

Mandal, R., R.M. Samstein, K.W. Lee, J.J. Havel, H. Wang, C. Krishna, E.Y. Sabio, V. Makarov, F. Kuo, P. Blecua, et al. 2019. Genetic diversity of tumors with mismatch repair deficiency influences anti-PD-1 immunotherapy response. *Science.* 364:485–491. https://doi.org/10.1126/science.aau0447

Marijt, K.A., M. Sluijter, L. Blijleven, S.H. Tolmeijer, F.A. Scheeren, S.H. van der Burg, and T. van Hall. 2019. Metabolic stress in cancer cells induces immune escape through a PI3K-dependent blockade of IFNγ receptor signaling. *J. Immunother. Cancer.* 7:152. https://doi.org/10.1186/s40425-019-0627-8

Martinez-Usatorre, A., E. Kadioglu, G. Boivin, C. Cianciaruso, A. Guichard, B. Torchia, N. Zangger, S. Nassiri, I. Keklikoglou, M. Schmittnaegel, et al. 2021. Overcoming microenvironmental resistance to PD-1 blockade in genetically engineered lung cancer models. *Sci. Transl. Med.* 13:eabd1616. https://doi.org/10.1126/scitranslmed.abd1616

McGranahan, N., A.J. Furness, R. Rosenthal, S. Ramskov, R. Lyngaa, S.K. Saini, M. Jamal-Hanjani, G.A. Wilson, N.J. Birkbak, C.T. Hiley, et al. 2016. Clonal neoantigens elicit T cell immunoreactivity and sensitivity to immune checkpoint blockade. *Science.* 351:1463–1469. https://doi.org/10.1126/science.aaf1490

McNeal, K.C., K.M. Reeves, P.N. Song, S.E. Lapi, A.G. Sorace, and B.M. Larimer. 2024. [^{18}F]FMISO-PET imaging reveals the role of hypoxia severity in checkpoint blockade response. *Nucl. Med. Biol.* 134-135:108918. https://doi.org/10.1016/j.nucmedbio.2024.108918

Memon, D., A.J. Schoenfeld, D. Ye, G. Fromm, H. Rizvi, X. Zhang, M.R. Keddar, D. Mathew, K.J. Yoo, J. Qiu, et al. 2024. Clinical and molecular features of acquired resistance to immunotherapy in non-small cell lung cancer. *Cancer Cell.* 42:209–224.e9. https://doi.org/10.1016/j.ccell.2023.12.013

Meng, F., J.W. Evans, D. Bhupathi, M. Banica, L. Lan, G. Lorente, J.X. Duan, X. Cai, A.M. Mowday, C.P. Guise, et al. 2012. Molecular and cellular pharmacology of the hypoxia-activated prodrug TH-302. *Mol. Cancer Ther.* 11:740–751. https://doi.org/10.1158/1535-7163.MCT-11-0634

Minassian, L.M., T. Cotechini, E. Huitema, and C.H. Graham. 2019. Hypoxia-induced resistance to chemotherapy in cancer. *In* Hypoxia and Cancer Metastasis. Vol. 1136. D.M. Gilkes, editor. Springer International Publishing, Cham, Switzerland. 123–139. https://doi.org/10.1007/978-3-030-12734-3_9

Murthy, A., S.A. Gerber, C.J. Koch, and E.M. Lord. 2019. Intratumoral hypoxia reduces IFN-γ-Mediated immunity and MHC class I induction in a preclinical tumor model. *Immunohorizons.* 3:149–160. https://doi.org/10.4049/immunohorizons.1900017

Najjar, Y.G., A.V. Menk, C. Sander, U. Rao, A. Karunamurthy, R. Bhatia, S. Zhai, J.M. Kirkwood, and G.M. Delgoffe. 2019. Tumor cell oxidative metabolism as a barrier to PD-1 blockade immunotherapy in melanoma. *JCI Insight.* 4:e124989. https://doi.org/10.1172/jci.insight.124989

Park, J.H., H.J. Kim, C.W. Kim, H.C. Kim, Y. Jung, H.S. Lee, Y. Lee, Y.S. Ju, J.E. Oh, S.H. Park, et al. 2021. Tumor hypoxia represses γδ T cell-mediated antitumor immunity against brain tumors. *Nat. Immunol.* 22:336–346. https://doi.org/10.1038/s41590-020-00860-7

Planchard, D., S. Popat, K. Kerr, S. Novello, E.F. Smit, C. Faivre-Finn, T.S. Mok, M. Reck, P.E. Van Schil, M.D. Hellmann, et al. 2018. Metastatic non-small cell lung cancer: ESMO clinical practice guidelines for diagnosis, treatment and follow-up. *Ann. Oncol.* 29:iv192–iv237. https://doi.org/10.1093/annonc/mdy275

Pouysségur, J., F. Dayan, and N.M. Mazure. 2006. Hypoxia signalling in cancer and approaches to enforce tumour regression. *Nature.* 441:437–443. https://doi.org/10.1038/nature04871

Ravi, A., M.D. Hellmann, M.B. Arniella, M. Holton, S.S. Freeman, V. Naranbhai, C. Stewart, I. Leshchiner, J. Kim, Y. Akiyama, et al. 2023. Genomic and transcriptomic analysis of checkpoint blockade response in advanced non-small cell lung cancer. *Nat. Genet.* 55:807–819. https://doi.org/10.1038/s41588-023-01355-5

Reck, M., D. Rodríguez-Abreu, A.G. Robinson, R. Hui, T. Csőszi, A. Fülöp, M. Gottfried, N. Peled, A. Tafreshi, S. Cuffe, et al. 2016. Pembrolizumab versus chemotherapy for PD-L1-positive non-small-cell lung cancer. *N. Engl. J. Med.* 375:1823–1833. https://doi.org/10.1056/NEJMoa1606774

Reeves, K.M., P.N. Song, A. Angermeier, D. Della Manna, Y. Li, J. Wang, E.S. Yang, A.G. Sorace, and B.M. Larimer. 2022. ^{18}F-FMISO PET imaging identifies hypoxia and immunosuppressive tumor microenvironments and guides targeted evofosfamide therapy in tumors refractory to PD-1 and CTLA-4 inhibition. *Clin. Cancer Res.* 28:327–337. https://doi.org/10.1158/1078-0432.CCR-21-2394

Ricciuti, B., G. Lamberti, S.R. Puchala, N.R. Mahadevan, J.R. Lin, J.V. Alessi, A. Chowdhury, Y.Y. Li, X. Wang, L. Spurr, et al. 2024. Genomic and immunophenotypic landscape of acquired resistance to PD-(L)1 blockade in non-small-cell lung cancer. *J. Clin. Oncol.* 42:1311–1321. https://doi.org/10.1200/JCO.23.00580

Rizvi, N.A., M.D. Hellmann, A. Snyder, P. Kvistborg, V. Makarov, J.J. Havel, W. Lee, J. Yuan, P. Wong, T.S. Ho, et al. 2015. Cancer immunology. Mutational landscape determines sensitivity to PD-1 blockade in non-small cell lung cancer. *Science.* 348:124–128. https://doi.org/10.1126/science.aaa1348

Rousseau, B., M.B. Foote, S.B. Maron, B.H. Diplas, S. Lu, G. Argilés, A. Cercek, and L.A. Diaz Jr. 2021. The spectrum of benefit from checkpoint blockade in hypermutated tumors. *N. Engl. J. Med.* 384:1168–1170. https://doi.org/10.1056/NEJMc2031965

Sade-Feldman, M., K. Yizhak, S.L. Bjorgaard, J.P. Ray, C.G. de Boer, R.W. Jenkins, D.J. Lieb, J.H. Chen, D.T. Frederick, M. Barzily-Rokni, et al. 2018. Defining T cell states associated with response to checkpoint immunotherapy in melanoma. *Cell.* 175:998–1013.e20. https://doi.org/10.1016/j.cell.2018.10.038

Samstein, R.M., C.H. Lee, A.N. Shoushtari, M.D. Hellmann, R. Shen, Y.Y. Janjigian, D.A. Barron, A. Zehir, E.J. Jordan, A. Omuro, et al. 2019. Tumor mutational load predicts survival after immunotherapy across multiple cancer types. *Nat. Genet.* 51:202–206. https://doi.org/10.1038/s41588-018-0312-8

Scharping, N.E., A.V. Menk, R.D. Whetstone, X. Zeng, and G.M. Delgoffe. 2017. Efficacy of PD-1 blockade is potentiated by metformin-induced reduction of tumor hypoxia. *Cancer Immunol. Res.* 5:9–16. https://doi.org/10.1158/2326-6066.CIR-16-0103

Schoenfeld, A.J., S.J. Antonia, M.M. Awad, E. Felip, J. Gainor, S.N. Gettinger, F.S. Hodi, M.L. Johnson, N.B. Leighl, C.M. Lovly, et al. 2021. Clinical definition of acquired resistance to immunotherapy in patients with metastatic non-small-cell lung cancer. *Ann. Oncol.* 32:1597–1607. https://doi.org/10.1016/j.annonc.2021.08.2151

Schoenfeld, A.J., and M.D. Hellmann. 2020. Acquired resistance to immune checkpoint inhibitors. *Cancer Cell.* 37:443–455. https://doi.org/10.1016/j.ccell.2020.03.017

Sirois, I., M. Isabelle, J.D. Duquette, F. Saab, and E. Caron. 2021. Immunopeptidomics: Isolation of mouse and human MHC class I- and II-associated peptides for mass spectrometry analysis. *J. Vis. Exp.* https://doi.org/10.3791/63052-v

Skoulidis, F., M.E. Goldberg, D.M. Greenawalt, M.D. Hellmann, M.M. Awad, J.F. Gainor, A.B. Schrock, R.J. Hartmaier, S.E. Trabucco, L. Gay, et al. 2018. STK11/LKB1 mutations and PD-1 inhibitor resistance in KRAS-mutant lung adenocarcinoma. *Cancer Discov.* 8:822–835. https://doi.org/10.1158/2159-8290.CD-18-0099

Sucker, A., F. Zhao, N. Pieper, C. Heeke, R. Maltaner, N. Stadtler, B. Real, N. Bielefeld, S. Howe, B. Weide, et al. 2017. Acquired IFNγ resistance impairs anti-tumor immunity and gives rise to T-cell-resistant melanoma lesions. *Nat. Commun.* 8:15440. https://doi.org/10.1038/ncomms15440

Supek, F., and B. Lehner. 2015. Differential DNA mismatch repair underlies mutation rate variation across the human genome. *Nature.* 521:81–84. https://doi.org/10.1038/nature14173

Torrejon, D.Y., G. Abril-Rodriguez, A.S. Champhekar, J. Tsoi, K.M. Campbell, A. Kalbasi, G. Parisi, J.M. Zaretsky, A. Garcia-Diaz, C. Puig-Saus, et al. 2020. Overcoming genetically based resistance mechanisms to PD-1 blockade. *Cancer Discov.* 10:1140–1157. https://doi.org/10.1158/2159-8290.CD-19-1409

Tumeh, P.C., C.L. Harview, J.H. Yearley, I.P. Shintaku, E.J. Taylor, L. Robert, B. Chmielowski, M. Spasic, G. Henry, V. Ciobanu, et al. 2014. PD-1 blockade induces responses by inhibiting adaptive immune resistance. *Nature.* 515:568–571. https://doi.org/10.1038/nature13954

Vaupel, P., and A. Mayer. 2007. Hypoxia in cancer: Significance and impact on clinical outcome. *Cancer Metastasis Rev.* 26:225–239. https://doi.org/10.1007/s10555-007-9055-1

Walsh, J.C., A. Lebedev, E. Aten, K. Madsen, L. Marciano, and H.C. Kolb. 2014. The clinical importance of assessing tumor hypoxia: Relationship of tumor hypoxia to prognosis and therapeutic opportunities. *Antioxid. Redox Signal.* 21:1516–1554. https://doi.org/10.1089/ars.2013.5378

Westcott, P.M.K., F. Muyas, H. Hauck, O.C. Smith, N.J. Sacks, Z.A. Ely, A.M. Jaeger, W.M. Rideout III, D. Zhang, A. Bhutkar, et al. 2023. Mismatch repair deficiency is not sufficient to elicit tumor immunogenicity. *Nat. Genet.* 55:1686–1695. https://doi.org/10.1038/s41588-023-01499-4

Wilson, W.R., and M.P. Hay. 2011. Targeting hypoxia in cancer therapy. *Nat. Rev. Cancer*. 11:393–410. https://doi.org/10.1038/nrc3064

Winslow, M.M., T.L. Dayton, R.G. Verhaak, C. Kim-Kiselak, E.L. Snyder, D.M. Feldser, D.D. Hubbard, M.J. DuPage, C.A. Whittaker, S. Hoersch, et al. 2011. Suppression of lung adenocarcinoma progression by Nkx2-1. *Nature*. 473:101–104. https://doi.org/10.1038/nature09881

Wislez, M., M.L. Spencer, J.G. Izzo, D.M. Juroske, K. Balhara, D.D. Cody, R.E. Price, W.N. Hittelman, I.I. Wistuba, and J.M. Kurie. 2005. Inhibition of mammalian target of rapamycin reverses alveolar epithelial neoplasia induced by oncogenic K-ras. *Cancer Res.* 65:3226–3235. https://doi.org/10.1158/0008-5472.CAN-04-4420

Wolf, Y., O. Bartok, S. Patkar, G.B. Eli, S. Cohen, K. Litchfield, R. Levy, A. Jiménez-Sánchez, S. Trabish, J.S. Lee, et al. 2019. UVB-induced tumor heterogeneity diminishes immune response in melanoma. *Cell*. 179: 219–235.e21. https://doi.org/10.1016/j.cell.2019.08.032

Wu, L., K. Li, B. Chen, W. Peng, J. Wang, M. Jiang, Q. Wang, X. Pu, J. Li, F. Xu, and Y. Xu. 2021. P48.15 A case from a single-arm, phase two, open label study assessing sindilimab plus metaformin in chemotherapy failed PD-L1 positive advanced SCLC. *J. Thorac. Oncol.* 16:S505–S506. https://doi.org/10.1016/j.jtho.2021.01.885

Zandberg, D.P., A.V. Menk, M. Velez, D. Normolle, K. DePeaux, A. Liu, R.L. Ferris, and G.M. Delgoffe. 2021. Tumor hypoxia is associated with resistance to PD-1 blockade in squamous cell carcinoma of the head and neck. *J. Immunother. Cancer*. 9:e002088. https://doi.org/10.1136/jitc-2020-002088

Zaretsky, J.M., A. Garcia-Diaz, D.S. Shin, H. Escuin-Ordinas, W. Hugo, S. Hu-Lieskovan, D.Y. Torrejon, G. Abril-Rodriguez, S. Sandoval, L. Barthly, et al. 2016. Mutations associated with acquired resistance to PD-1 blockade in melanoma. *N. Engl. J. Med.* 375:819–829. https://doi.org/10.1056/NEJMoa1604958

Supplemental material

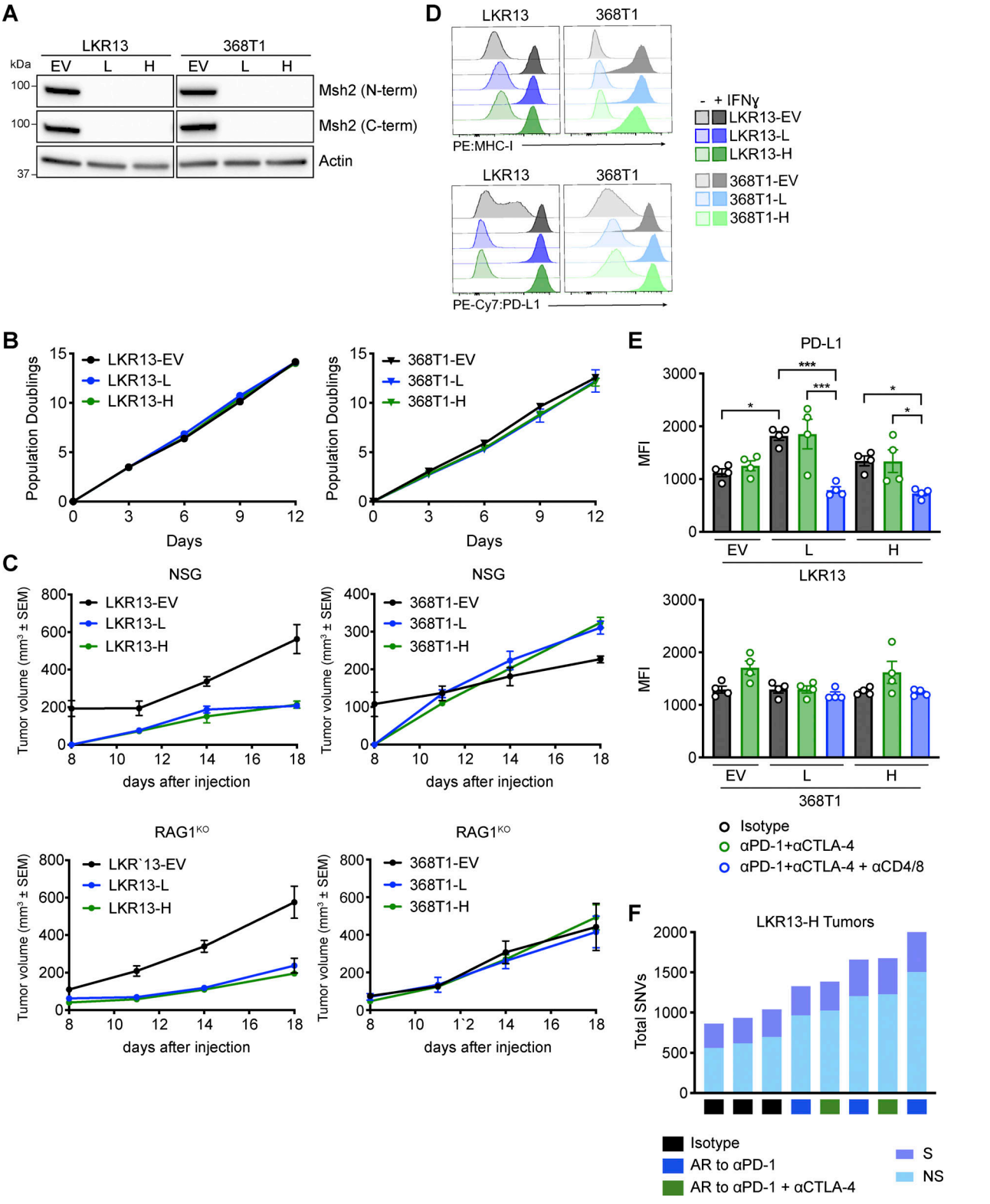

Figure S1. **Validation of *Msh2* KO tumors. (A)** Immunoblot analysis of C-terminal and N-terminal Msh2 expression in EV and *Msh2* KO (L and H) LKR13 and 368T1 cells; β-Actin is a loading control; data shown are representative of two independent experiments. **(B)** In vitro proliferation assay of EV and *Msh2* KO (L and H) cells. **(C)** Tumor growth curves after 500,000 of the indicated cells were injected subcutaneously into NSG (top) and Rag1^{KO} (bottom) mice (n = 3–4 mice per group). **(D)** Surface expression of MHC-I and PD-L1 in EV and *Msh2* KO (L and H) cells with and without IFNγ treatment in vitro. **(E)** Expression of PD-L1 in CD45^{-} cancer (and stromal) cells from EV and *Msh2* KO (L and H) LKR13 (top) and 368T1 (bottom) tumors on day 22 after tumor initiation in immunocompetent B6129SF1/J mice (n = 4 mice per group). **(F)** Number of synonymous (S) and non-synonymous (NS) SNVs identified in *Msh2* KO LKR13-H tumors collected from B6129SF1/J mice that were either treated with Iso, or were treated with and developed AR to anti-PD-1 or anti-PD-1 and anti-CTLA-4. Significance was determined using one-way ANOVA (E). *P < 0.05, ***P < 0.001. Source data are available for this figure: SourceData FS1.

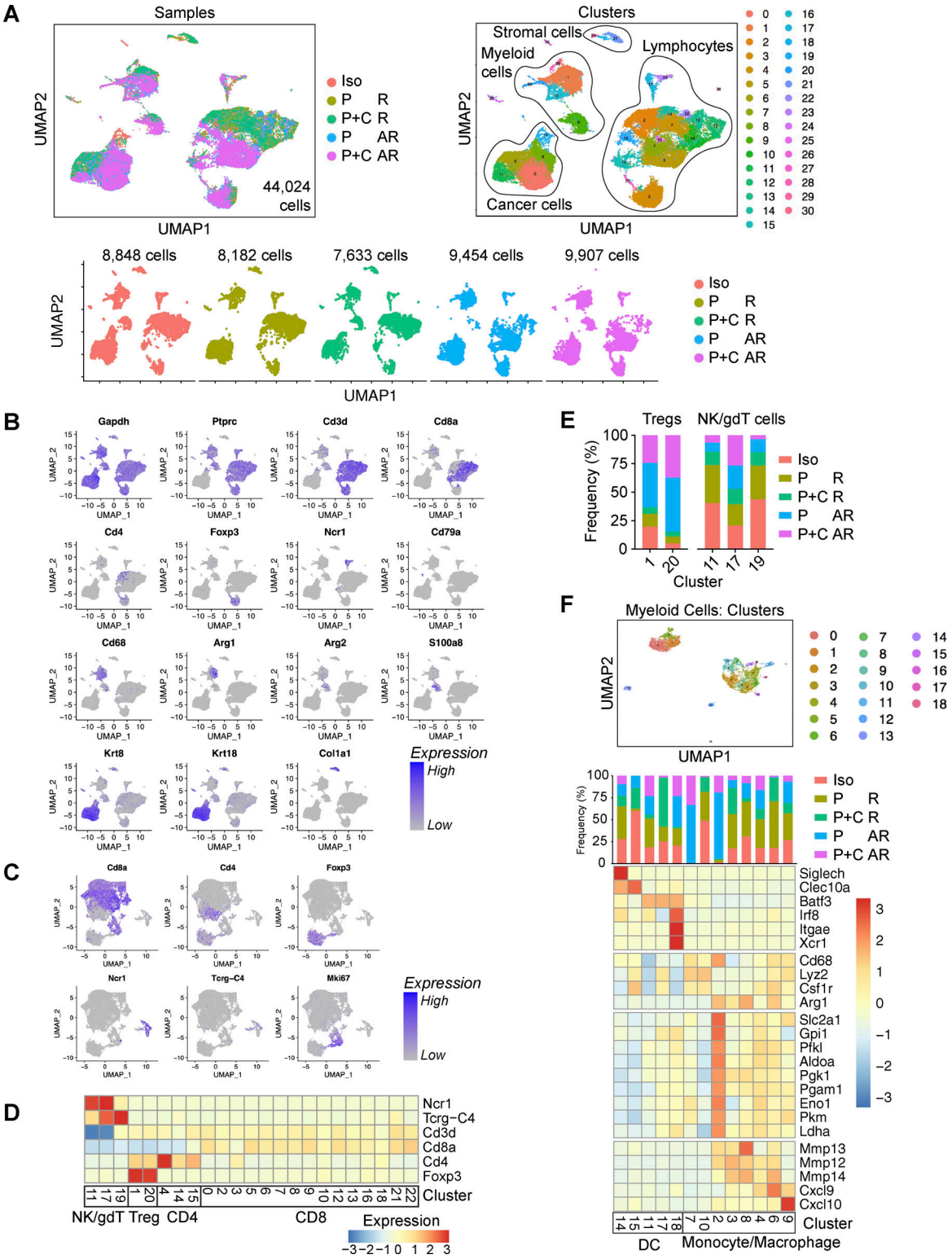

Figure S2. **Single-cell RNA sequencing reveals broad differences in cancer cells and the immune microenvironment between responding and resistant tumors. (A)** UMAP projection of cells isolated from LKR13-H tumors colored by treatment condition (top left) and cluster (top right) showing 44,024 cells total and split by treatment condition showing the number of cells per treatment (bottom). **(B)** UMAP projection of all cells analyzed depicting expression of genes that were used to support cell-type assignments shown in A, top right panel. **(C)** UMAP projection depicting expression of selected genes in lymphocytes from A that were computationally isolated and re-clustered as shown in Fig. 3 C. **(D)** Heatmap showing mean expression of selected genes in lymphocyte clusters from Fig. 3 C. **(E)** Percentage of cells in Treg and natural killer (NK)/γδT cell clusters from D by treatment condition. **(F)** UMAP projection showing sub-clustered myeloid cells from LKR13-H tumors shown in A colored by cluster (top) and percentage of cells in each cluster by treatment condition (middle) and heatmap showing mean expression of selected genes (bottom) in DCs (clusters 14, 15, 11, 17, 18) and monocytes/macrophages (clusters 7, 10, 2, 3, 8, 4, 6, 9) computationally sub-clustered from A. R, responding; P, anti-PD-1; P+C, anti-PD-1 + anti-CTLA-4.

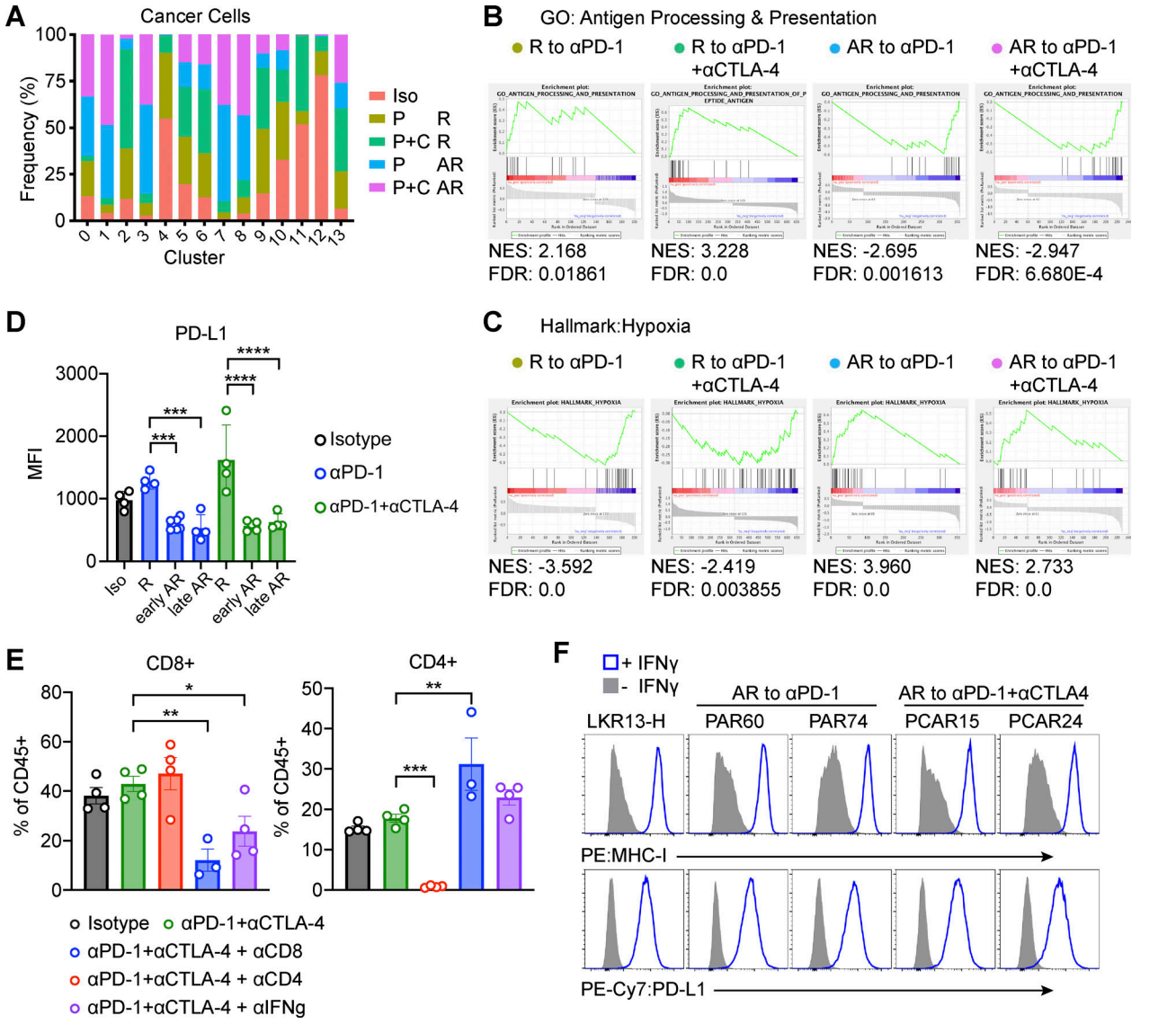

Figure S3. **Cancer cells in resistant tumors have elevated hypoxia and reduced antigen processing and presentation. (A)** Percentage of cells by treatment condition in cancer cell clusters. **(B)** GSEA profiles showing enrichment for the GO Antigen Processing & Presentation gene set in cancer cells from tumors responding (R) to anti-PD-1 or anti-PD-1 + anti-CTLA-4 but not those with AR to therapy. **(C)** GSEA profiles showing enrichment for the Hallmark Hypoxia gene set in cancer cells from tumors with AR to anti-PD-1 or anti-PD-1 + anti-CTLA-4 but not those responding to therapy. False discovery rate (FDR); Normalized enrichment score (NES). **(D)** Expression of PD-L1 in $CD45^-$ cancer (and stromal) cells isolated from LKR13-H tumors collected from isotype-treated B6129SF1/J mice (Iso) and mice that were responding (R) to either anti-PD-1 (P) or anti-PD-1 + anti-CTLA-4 (P+C) therapy on day 16, and mice that developed AR to therapy either on day 26 (early AR) or day 39 (late AR) (n = 4–7 mice per group). **(E)** Abundance of $CD8^+$ (left) and $CD4^+$ (right) T cells in LKR13-H tumors treated with isotype or anti-PD-1 + anti-CTLA-4 and with either anti-CD4, anti-CD8 or anti-IFNγ antibodies twice weekly starting on day 10 and collected on day 22 (n = 3–4 mice per group). **(F)** Surface expression of MHC-I (top) and PD-L1 (bottom) after in vitro IFNγ stimulation in LKR13-H cells and four cell lines derived from LKR13-H tumors that developed AR to either anti-PD-1 (PAR60, PAR74) or anti-PD-1 and anti-CTLA-4 (PCAR15, PCAR24). Significance was determined using one-way ANOVA (D and E). *P < 0.05, **P < 0.01, ***P < 0.001, ****P < 0.0001.

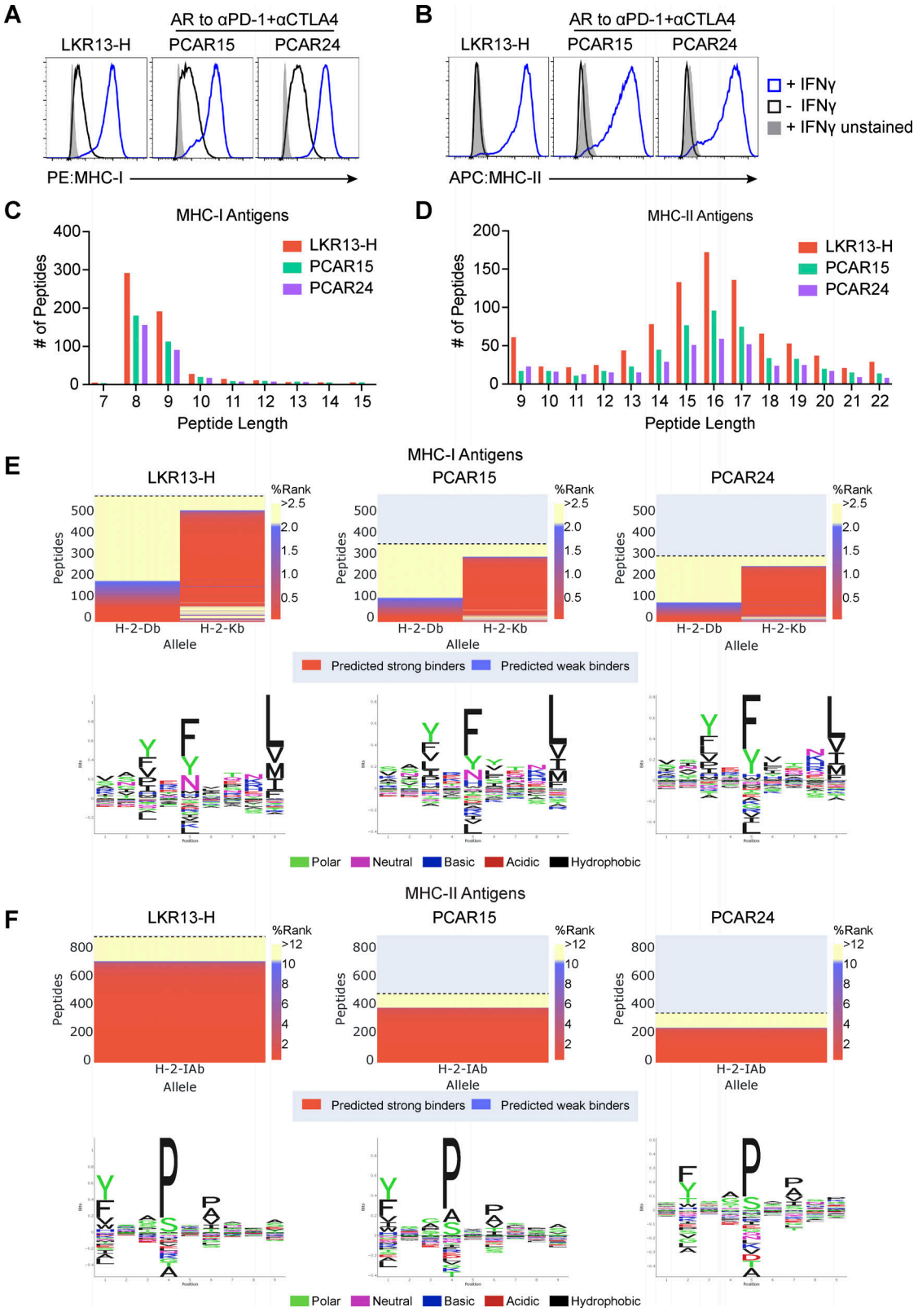

Figure S4. **Decrease in the abundance of peptides presented on MHC in resistant cancer cells. (A and B)** Surface expression of MHC-I (A) and MHC-II (B) after in vitro IFNγ stimulation in *Msh2* KO LKR13-H cells and two cell lines derived from LKR13-H tumors that developed acquired resistance to anti-PD-1 and anti-CTLA-4 (PCAR15, PCAR24); data shown are representative of two independent experiments. Immunopeptidome analysis was performed on IFNγ-treated cells to eliminate the confounding effects of differences in MHC expression. **(C and D)** Length distribution of eluted peptides bound to MHC-I (C) and MHC-II (D). **(E and F)** Heatmaps showing the number of peptides with binding affinity scores for H-2D^b and H-2K^b MHC-I alleles (E) and H-2IA^b MHC-II alleles (F) for each cell line (top). Peptide binding motifs based on unsupervised GibbsCluster analysis for each cell line (bottom).

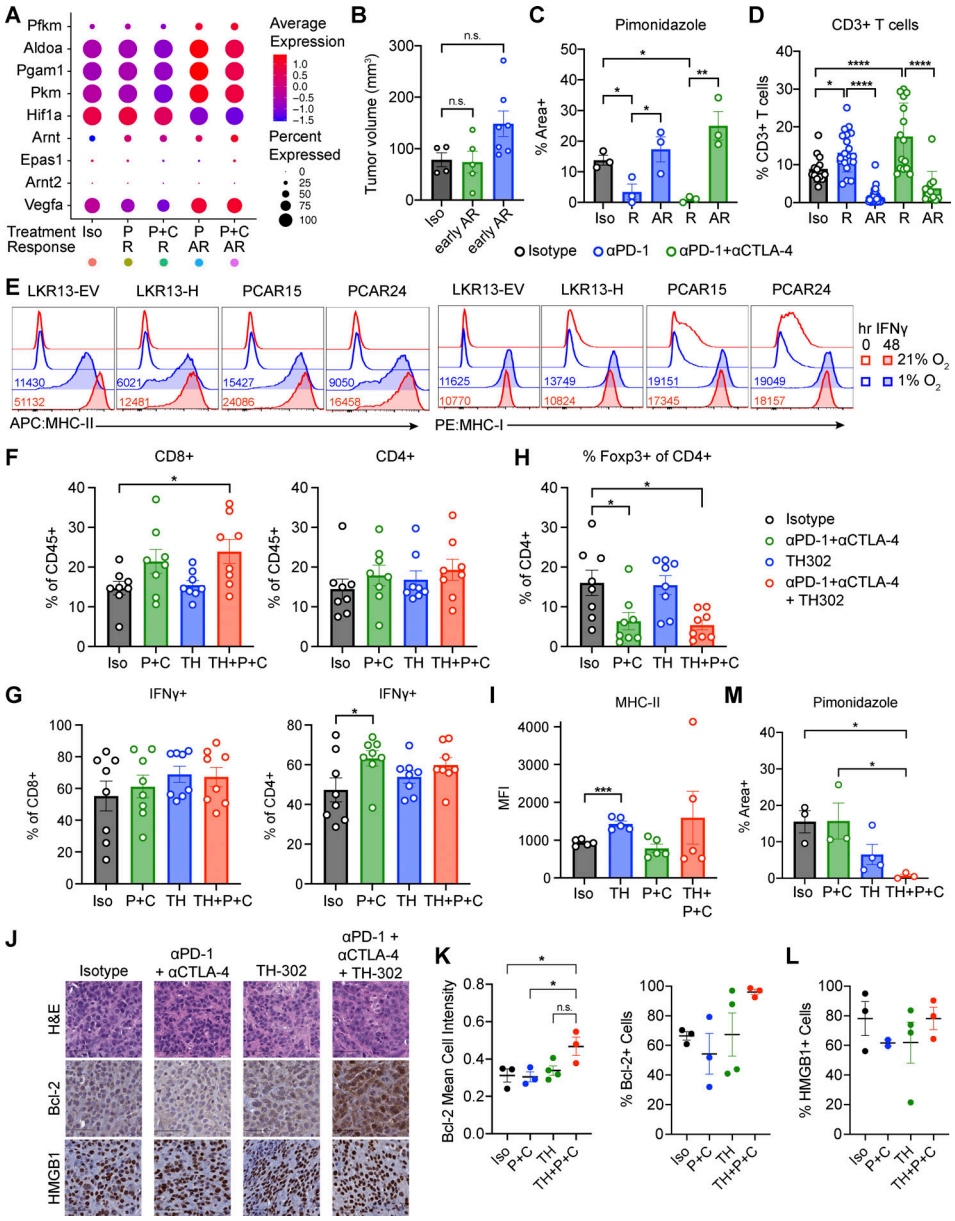

Figure S5. **Hypoxia in tumors with acquired resistance to ICIs can be targeted with TH-302. (A)** Dotplot showing the expression of additional glycolytic enzymes (*Pfkm*, *Aldoa*, *Pgam1*, and *Pkm*) as well as *Hif1a*, *Arnt*, *Epas1*, *Arnt2*, and *Vegfa* in cancer cells by treatment condition (related to Fig. 6 A). **(B)** Final volumes for isotype-treated tumors from B6129SF1/J mice collected on day 16 (Iso) and tumors from mice with AR to anti-PD-1 or anti-PD-1 + anti-CTLA-4 collected on day 26 (early AR). **(C and D)** Immunofluorescence staining for pimonidazole (FITC, green) and CD3 (Alexa Fluor 594, red) in LKR13-H tumors collected from mice treated with Iso and mice that were responding (R) to either anti-PD-1 (P) or anti-PD-1 + anti-CTLA-4 (P+C) therapy on day 16 and mice that developed AR to therapy on day 39 (n = 3 mice per group). **(C)** Average percent hypoxic (pimonidazole+) area per tumor quantified using QuPath. **(D)** Percentage of CD3⁺ T cells quantified using QuPath from at least three FOV per tumor. **(E)** Representative histograms showing expression of MHC-II and MHC-I after in vitro IFNγ stimulation under 21% oxygen (normoxia) or 1% oxygen (hypoxia) in *Msh2* WT LKR13-EV cells, *Msh2* KO LKR13-H cells, and two cell lines derived from LKR13-H tumors that developed AR to anti-PD-1 and anti-CTLA-4 (PCAR15, PCAR24). Mean fluorescence intensities (MFIs) are labeled for IFNγ-treated samples. **(F–M)** Mice harboring LKR13-H tumors were treated with either Iso or anti-PD-1 and anti-CTLA-4 twice weekly and/or with TH-302 every other day starting on day 10 after tumor initiation. **(F–H)** Abundance of CD8⁺ (left) and CD4⁺ (right) T cells (F), IFNγ secretion after ex vivo stimulation in CD8⁺ (left) and CD4⁺ (right) T cells (G), and abundance of Foxp3⁺ Tregs (H) in LKR13-H tumors collected on day 16. Data is pooled from two independent experiments with four mice per group (total eight mice per group). **(I)** Expression of MHC-II in CD45⁻ cancer (and stromal) cells in LKR13-H tumors collected on day 39 (isotype and TH302) or day 53 (anti-PD-1 + anti-CTLA-4 and TH302 + anti-PD-1 + anti-CTLA-4). Data is representative of two independent experiments with three to four or five mice per group. **(J–L)** Immunohistochemistry staining in LKR13-H tumors collected from mice treated with Iso or anti-PD-1 + anti-CTLA-4 and/or with TH-302 (n = 3–4 mice per group). **(J)** Representative images of H&E (top), Bcl-2 (middle), and HMGB1 (bottom). Scale bars, 50 µm. **(K and L)** Quantification using QuPath of mean Bcl-2 cell intensity (left) and percent cells expressing Bcl-2 (right) (K) and percent cells expressing HMGB1 (L). **(M)** Average percent hypoxic (pimonidazole+) area per tumor quantified using QuPath from immunofluorescence staining for pimonidazole (FITC, green) in LKR13-H tumors collected from mice treated with Iso or anti-PD-1 + anti-CTLA-4 and/or with TH-302 (n = 3–4 mice per group). Significance was determined using one-way ANOVA (B–D, F–H, and K–M) or un-paired two-tailed Student's t test (I). *P < 0.05, **P < 0.01, ***P < 0.001, ****P < 0.0001, n.s., not significant.

Provided online is Table S1. Table S1 shows significantly (FDR q value <0.25; P value <0.05) enriched GO and Hallmark gene sets in cancer cells from LKR13-H tumors responding (R) or with AR to anti-PD-1 (P) or anti-PD-1+anti-CTLA-4 (P+C).